Politecnico di Torino

Master's Degree in Biomedical Engineering
A.a. 2024/2025
Graduation Session July 2025

Design and fabrication of piezoelectric cardiac patches with auxetic geometry for myocardial repair

Supervisor:
Valeria Chiono
Michael Monaghan

Candidates:
Antonio Pellico

Abstract

Myocardial infarction (MI) is a major contributor to global mortality, impairing heart function by inducing extensive loss of cardiomyocytes and isolation of the remaining cells within a fibrotic scar tissue. Among emerging regenerative pathways, cardiac patches represent a promising approach for myocardial regeneration, as studies have demonstrated their capacity to support cellular regeneration by providing mechanical reinforcement or facilitating electrical conductivity. However, many existing designs fail to integrate both functionalities, which are essential for optimal cardiac tissue repair. Piezoelectric materials are particularly suited for this purpose, due to their ability to generate electrical fields in response to mechanical actuation, and the potential to adapt to match the anisotropic motion of the cardiac chambers. This research project aims to achieve the integration of both an auxetic patch geometry and piezoelectric functionality in a cardiac patch with tuneable properties, with the dual goal of establishing a pipeline for comparing auxetic designs and laying the groundwork towards the integration of piezoelectric properties. Medical-grade PCL (PCL) patches were fabricated via melt electrowriting (MEW) to determine how printing and geometric parameters affect mechanical properties, assessed through monotonic tensile testing. Specifically, patches with varying layer counts and mesh sizes were compared using Young's modulus and Poisson's ratio as key metrics. A custom MATLAB application was developed to extract the Poisson's ratio of the meshes from videos acquired during mechanical testing. As both the number of layers and mesh size had an impact on the Young's modulus, the mechanical performance of different auxetic geometries (lozenge truss, arrowhead and missing rib) was finally evaluated by testing patches of the same dimensions and layer count. Piezoelectricity was introduced by coating the patches with polyvinylidene fluoride (PVDF) or polyvinylidene fluoride - hexafluoropropylene (PVDF-HFP) using a dip coating technique. Both coated and uncoated patches were subjected to cyclic and monotonic uniaxial testing, as well as scanning electron microscopy (SEM). Imaging before and after stretching assessed the stability of the coating, which persisted up to 40% strain. Piezoelectric properties were characterized using Fourier-transform infrared spectroscopy (FTIR), confirming the presence of the piezoelectric β phase in the PVDF. To assess cytocompatibility of the materials, indirect MTT assays were performed on human induced pluripotent stem cell (iPSC) - derived fibroblasts and primary human macrophages. In conclusion, this project offers valuable insight into the fabrication and mechanical characterization of melt electrowritten auxetic patches, while establishing a foundation for the integration of piezoelectric functionality. These findings provide a framework for advancing multifunctional cardiac patches in future regenerative applications.

Table of Contents

List of Tables

List of Figures

Glossary

CSA Cross-sectional area

DBSCAN Density-Based Spatial Clustering of Applications with Noise

DMF Dimethylformamide

DMSO Dimethyl sulfoxide

DSC Differential Scanning Calorimetry

FBS Fetal Bovine Serum

FTIR Fourier Transform Infrared Spectroscopy

HFP Hexafluoropropylene

M-CSF Monocyte-Colony Stimulating Factor

MEW Melt Electrowriting

MTT 3-(4,5-dimethylthiazolyl-2)-2,5-diphenyltetrazolium bromide

Mw Molecular weight

P/S Penicillin/Streptomycin

PCL Polycaprolactone ,

PVDF Poly(vinylidene fluoride)

ROI Region of interest

SEM Scanning Electron Microscopy

Chapter 1

Introduction

Cardiovascular diseases (CVDs) are the leading cause of mortality worldwide, representing a major socioeconomic challenge. In the European Union alone, the annual cost associated with CVDs exceeds €200 billion [1]. The majority of CVD-related deaths, over 17.9 million annually, are due to myocardial infarction (MI) and stroke, driven by behavioural risk factors such as poor diet, physical inactivity, tobacco use, and excessive alcohol consumption [2].

MI is caused by occlusion of coronary arteries, leading to ischaemia, necrosis of contractile myocardium, and subsequent ventricular remodelling [3]. Due to the heart's limited regenerative capacity, the remodelling process involves wall thinning and deposition of fibrotic tissue, which significantly alters the myocardial microenvironment, causing increased stiffness and electrical insulation [4, 5, 6, 7] .

A variety of therapeutic strategies have been proposed to mitigate post-infarction remodelling, including engineered cardiac tissues. However, clinical translation has been hindered by poor cell engraftment and insufficient mechanical and electrical integration between patches and host tissue [8, 9]. To address these limitations, cardiac patches have emerged as a promising alternative, providing structural support and potentially enhancing electrical conduction [10].

It is widely accepted that the mechanical properties of biomaterials used to treat MI are of critical importance. Typically, cardiac patches are expected to mimic those of healthy native myocardial tissue, which exhibits a Young's modulus in the range of 0.02–0.5 MPa [11], and a Poisson's ratio between –0.2 and –0.5 [12]. To accommodate these unique mechanical characteristics, cardiac patches with auxetic geometries have been explored over the past two decades. Auxetic materials are defined by their negative Poisson's ratios, meaning they expand simultaneously in both axial and transverse directions when stretched [13]. Incorporating auxetic geometries into cardiac patches enables modulation of the material's mechanical response to better conform to the complex mechanics of the myocardium, including nonlinearity, viscoelasticity, and anisotropy [11, 12, 14].

Beyond mechanical integration, restoring electrical signalling across the infarcted region is pivotal for functional recovery. In this context, electroactive materials, particularly piezoelectric polymers, offer an attractive route for enhancing bioelectrical stimulation [14]. Piezoelectric materials generate electric charge in response to mechanical stress, a property exploited in the direct piezoelectric effect [15]. Among these, poly(vinylidene fluoride) (PVDF) is widely studied for its favourable piezoelectric response, particularly in its β-phase conformation [16, 17, 18] .

This project aims to achieve the integration of both an auxetic patch geometry and piezoelectric functionality in a cardiac patch with tuneable properties, with the dual goal of establishing a pipeline for comparing auxetic designs and laying the groundwork towards the integration of piezoelectric properties in a melt electrowritten cardiac scaffold for myocardial regeneration.

Chapter 2

Background

2.1 Myocardial infarction (MI)

CVDs are the leading cause of mortality worldwide, representing a major socioeconomic challenge. In the European Union alone, the annual cost associated with CVDs exceeds €200 billion [1]. In 2019, 85% of deaths caused by CVDs were due to myocardial infarction and stroke [1]. While the global mortality rate associated with MI has declined in recent years due to improved acute care, the incidence of heart failure (HF) following MI remains high, with persistent morbidity and mortality [19].

MI is typically caused by the rupture of a vulnerable atherosclerotic plaque or erosion of the coronary endothelium, leading to the release of thrombogenic contents, platelet activation, and thrombus formation. This cascade can culminate in occlusion of the coronary artery, resulting in ischaemia, myocardial cell death, and necrosis. It is estimated that an acute MI can result in the loss of approximately one billion cardiomyocytes in the left ventricular wall within hours of onset. [20, 21]. Given the limited regenerative capacity of the adult myocardium, the necrotic tissue is typically replaced by fibrotic scar tissue composed mainly of myofibroblasts and extracellular matrix [20]. This scar tissue is electrically unexcitable and mechanically stiff, impairing cardiac function and predisposing patients to arrhythmias, reduced contractility, recurrent infarctions, and progression to heart failure [22, 23]. Standard emergency treatment of MI involves reperfusion strategies, typically followed by percutaneous coronary intervention (PCI). This minimally invasive procedure involves catheter-based access to restore blood flow to the obstructed coronary artery. PCI is commonly complemented with pharmacotherapy, including antiplatelet agents, anticoagulants, and lipid-lowering drugs, to address the underlying pathophysiology and prevent further events. [24]

2.2 Cardiac patches

Cardiac patches have recently emerged as a promising strategy for MI therapy. They offer the potential to support cardiomyocyte regeneration, a particularly attractive goal given that many patients do not receive treatment early enough for maximal myocardial salvage, and that pharmacological interventions have yielded only modest improvements over the past decade [25]. Preclinical and clinical studies have shown that cell-based therapies can attenuate myocardial damage and slow the progression to heart failure. However, their efficacy is limited by poor cell retention and engraftment. Engineered heart tissues (EHTs), which aim to replicate the morphology and function of native myocardium, may overcome these limitations by leveraging biomaterials with stem or progenitor cells [8]. To be clinically effective, a cardiac patch must meet a set of stringent design criteria. It should provide mechanical support in response to the heart's multiaxial strain environment, facilitate electrical signal propagation, and foster cells along with growth factors. Furthermore, it should have a porous structure to allow for cell infiltration, neovascularisation, and tissue ingrowth. Manufacturability is also essential, as the scaffold must be customisable to patient-specific heart defects [26, 25]. As the field has evolved beyond initial proof-of-concept studies, advanced strategies have been introduced to engineer patches that more closely resemble the dynamic microenvironment of native myocardium. Two key approaches are the application of mechanical and electrical stimulation to enhance cell maturation and tissue functionality [8].

2.2.1 Mechanical stimulation

Mechanical stimulation has been shown to promote stem cell differentiation toward a cardiomyocyte lineage [27]. Various in vitro models have been developed to replicate the mechanical cues experienced by the myocardium, including shear stress [28], cyclic strain [29], hydrostatic pressure [30], and matrix stiffness [31]. [30] For successful integration, a cardiac patch must mimic the complex mechanical behaviour of the heart, including anisotropy, viscoelasticity, and non-linearity [14]. These properties vary throughout the cardiac cycle and are further altered following MI. The physiological stiffness of the left ventricle ranges from 31 kPa during early diastole to between 0.2 and 0.5 MPa at end-diastole [32], increasing further during post-infarct remodelling [33]. Passive myocardial strains can reach up to 22% at end-diastole [34], requiring patches to maintain elastic deformation within that range. Additionally, the native myocardium is anisotropic, with stiffness ratios (longitudinal/transverse) between 1.9 and 3.9 [11], and exhibits a negative Poisson's ratio, ranging from 0.2 to 0.5 [12].

2.2.2 Electrical stimulation

The myocardial contraction relies on the coordinated transmission of electrical impulses from pacemaker cells through cardiomyocytes via gap junctions and conductive pathways such as the Purkinje fibres. This electromechanical coupling is crucial for effective cardiac contraction and is often impaired following MI. [35] Transplantation of stem cell-derived cardiomyocytes in the infarcted area has shown promise in restoring function, however, these cells typically remain immature and exhibit poor electrical integration with host tissue, limiting their potential applications in the field. [36, 37] Electrical stimulation (ES) has recently gained interest as a non-pharmacological method to enhance maturation and functional properties of stem cell-derived cardiomyocytes [38]. ES can influence key parameters of differentiation, including cell alignment, contractile function, and electrophysiological synchrony. Factors such as pulse waveform, electric field intensity and duration, stimulation frequency, and onset timing all significantly affect outcomes [39]. Recent studies have also shown that ES enhances not only cardiomyocyte development, but also influences other cell types. For example, electrical stimulation of co-cultures containing iPSC-derived macrophages (iMacs) and iPSC-derived cardiomyocytes (iCMs) resulted in more mature cardiomyocyte phenotypes and a heightened regenerative response in iMacs [40]. These findings highlight the relevance of ES extends beyond cardiomyocytes to other resident cell populations in the myocardium. The therapeutic potential of ES underscores the need for cardiac patches to actively deliver electrical cues. One promising strategy is the incorporation of piezoelectric materials, a class of smart materials capable of generating electrical charges in response to mechanical deformation [15]. In the context of cardiac regeneration, the intrinsic motion of the beating heart could be harnessed to deform the piezoelectric scaffold, thereby producing bioelectrical stimulation in situ at physiological frequencies. This approach offers an elegant and self-sustaining solution to deliver functional electrical signals without relying on external devices or electrodes. [6, 41]

2.3 Auxetic designs

2.3.1 Definition of auxeticity

Poisson's ratio (PR) is defined as the ratio of transverse strain to longitudinal strain in the direction of applied tensile or compressive force. It is expressed as

$$\nu = -\frac{\epsilon_l}{\epsilon_a} \tag{2.1}$$

where ϵ_l is the lateral strain generated in response to the axial strain ϵ_a (along the loading direction) [42]. Due to the negative sign, conventional materials exhibit a positive PR: when stretched axially, they contract transversely. In contrast, materials that exhibit a negative PR are termed auxetic, meaning that transverse and longitudinal expansions occur simultaneously under tensile load (Figure 2.1) [43].

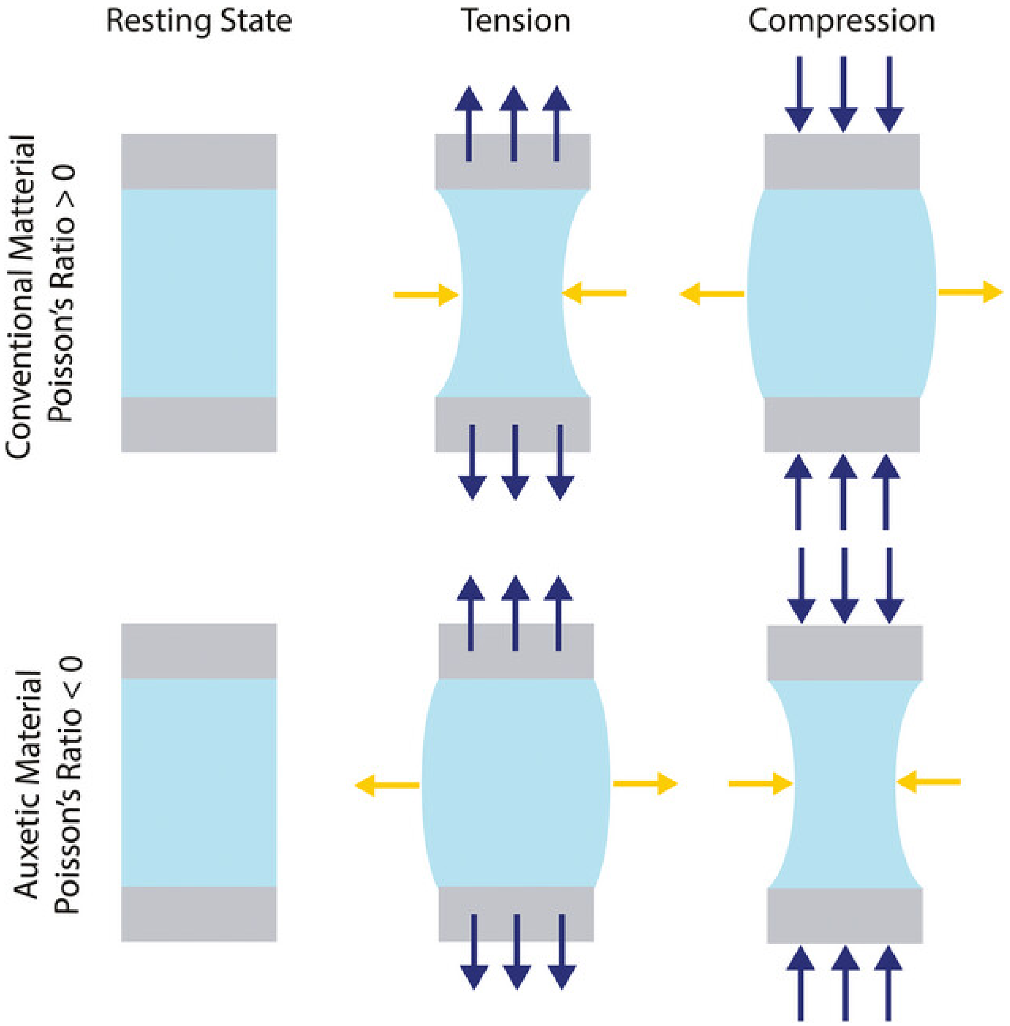

Figure 2.1: Schematic representation of positive and negative Poisson's ratios. Taken from [42]

.

2.3.2 Classification of auxetic designs

Based on the structural mechanisms responsible for their negative PR, auxetic designs are commonly classified into three main categories: re-entrant, chiral, and rotating structures [43].

Re-entrant unit cells

In 1987, Lakes introduced an idealised re-entrant unit cell to model auxetic foams. This unit cell was based on hexagonal honeycomb geometries derived by the symmetrical collapse of a 24-sided polyhedron exhibiting cubic symmetry (Figure 2.2a) [44]. Since then, re-entrant honeycomb designs have become one of the most extensively studied auxetic geometries [42]. The term “re-entrant” refers to inward direction or geometries having a negative angle [42]. In these designs, auxetic behaviour arises from expansion and rotation of the lines that compose the unit cells [43]. Due to their relatively simple structure and uniform pore size, re-entrant designs have been widely adopted in tissue engineering applications [42].

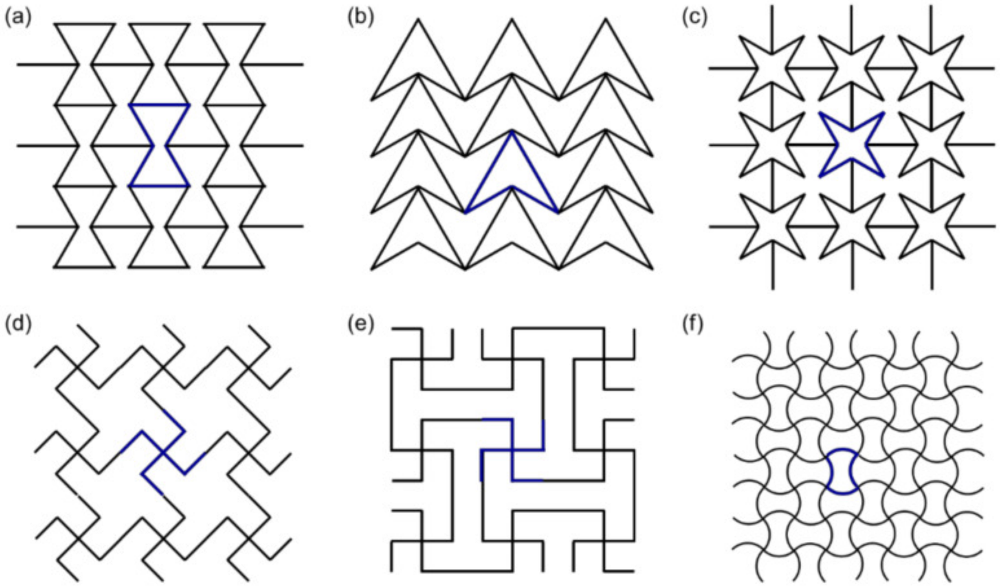

Figure 2.2: Re-entrant structures. (a) Re-entrant honeycomb. (b) Double arrowhead. (c) Star honeycomb. (d) Structurally hexagonal re-entrant honeycomb (or missing rib). (e) Lozenge grids (or lozenge truss). (f) Sinusoidal ligaments. Taken from [42]

.

Chiral unit cells

Chiral designs consist of a central node with tangentially connected ligaments, typically arranged in 3-, 4-, or 6-fold rotational symmetry (Figure 2.3) [45]. The configuration results in a chiral geometry, meaning the structure can exhibit either right-handed or left-handed orientation. The auxetic effect is induced when uniaxial stress generates torque, causing the ribs to rotate about the central node, leading to their wrapping or unwrapping [42].

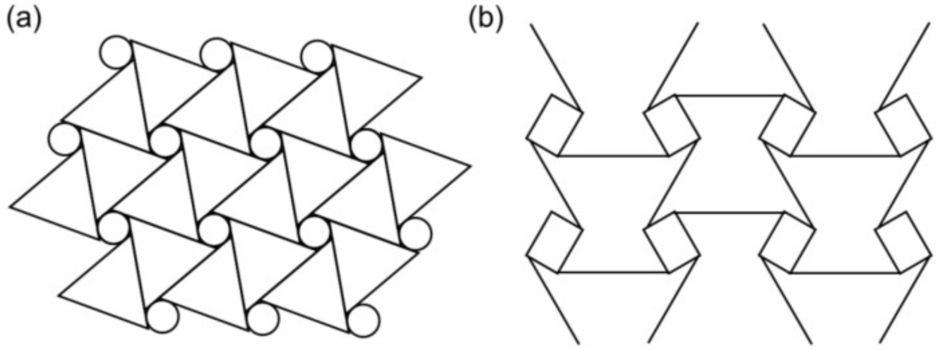

Figure 2.3: Chiral structures. (a) Chiral structure with same units. (b) Chiral structure with symmetrical units. Taken from [42]

.

Rotating unit cells

This class comprises structures built from rigid rotating units such as triangles, squares, or rectangles (Figure 2.4). Auxeticity arises from the rotation of these solid elements in response to mechanical loading. Unlike the beam- or ligament-based designs of other auxetic architectures, these structures rely on solid elements, leading to regions of 0% local porosity. This characteristic makes them less suitable for tissue engineering applications, as it may impair scaffold integration and hinder homogeneous tissue formation [42].

2.3.3 Auxetic designs in cardiac patches

Auxetic geometries have recently garnered significant attention in the development of cardiac patches. One of the primary drivers of this interest is the evidence that the human myocardium itself exhibits a negative Poisson's ratio [12]. Furthermore, auxetic structures offer high energy absorption, fracture resistance under cyclic loading, and improved mechanical performance in terms of shear resistance, indentation resistance, and synclastic curvature, all of which are beneficial for cardiac applications [46, 11]. Notably, stress–strain curves of collagen fibres exhibit a characteristic J-shaped profile (Figure 2.5). This curve comprises an initial non-linear toe region, attributed to the uncrimping of collagen fibrils, followed by a heel region and then a linear region. Because the uncrimping process requires less force, the toe region is associated with relatively low stiffness compared to the linear portion of the curve

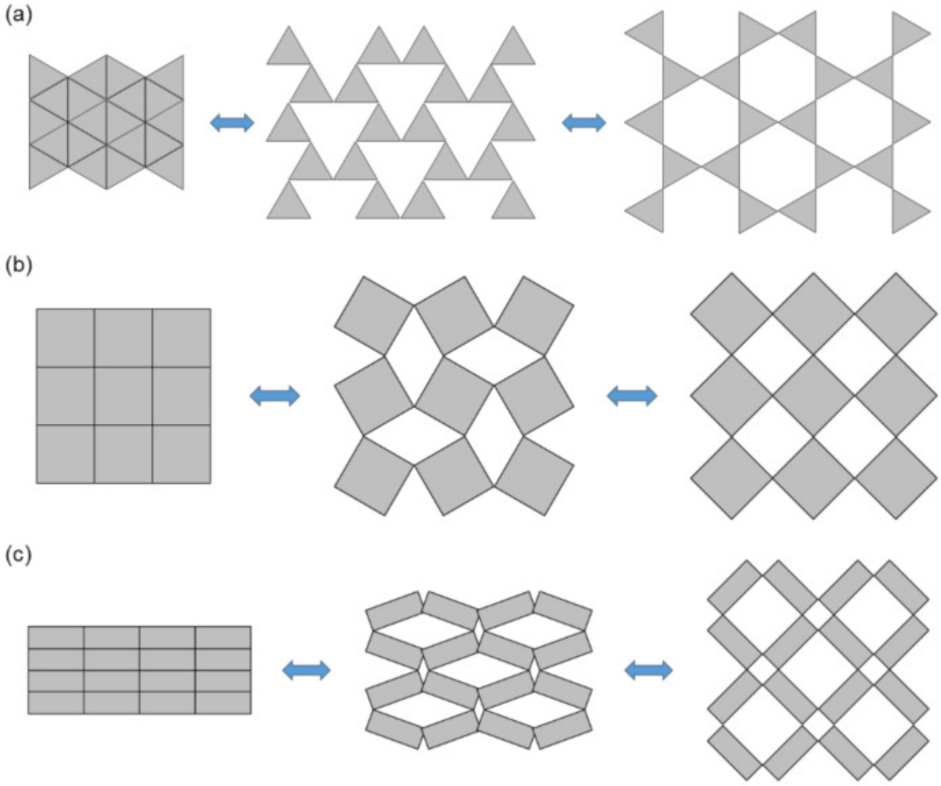

Figure 2.4: Rotating unit structures. (a) Triangle unit cells. (b) Square unit cell. (c) Rectangle unit cells. Taken from [42]

.

[47, 48]. Similar J-shaped profiles have been observed in a wide range of biological soft tissues [49], including the myocardium itself [50, 51]. Comparable stress–strain behaviours have been reported for certain auxetic designs. In these cases, the toe region corresponds to the unfolding or expansion of the geometric features within the structure, mimicking the crimped-to-aligned transition of collagen fibres [14, 52]. This similarity further reinforces the potential of auxetic patches to replicate the unique mechanical behaviour of native myocardial tissue.

A seminal contribution by Kapnisi et al. [11] involved the fabrication of an auxetic, conductive cardiac patch using microablation with an excimer laser. The patch was composed of a chitosan substrate functionalised with a conductive network of polyaniline and phytic acid. Due to the material's initial stiffness being significantly higher than native cardiac tissue [53], a re-entrant honeycomb geometry was introduced to tailor its mechanical properties. The resulting scaffold exhibited mechanical characteristics aligned with those of the myocardium, was cytocompatible with neonatal murine cardiomyocytes in vitro, and did not elicit

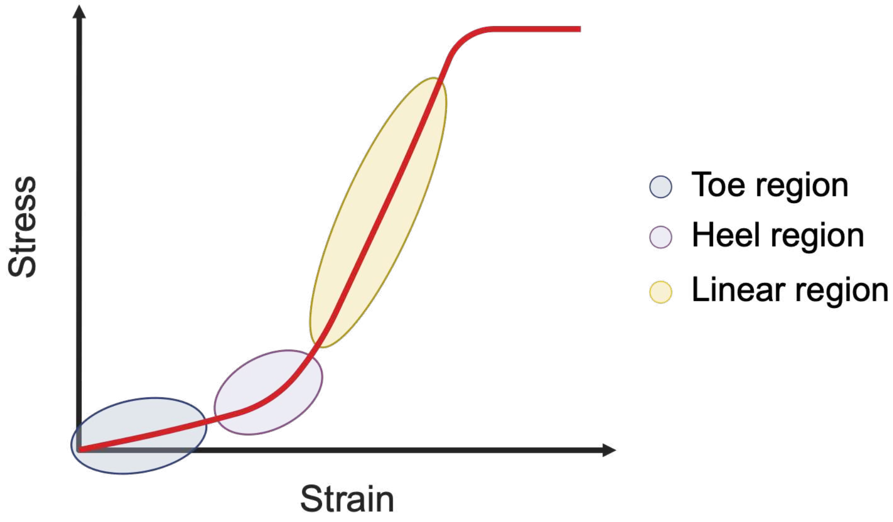

Figure 2.5: Schematic representation of J-shaped stress – strain curves.

fibrotic responses in vivo two weeks post-transplantation.

Another study on the development of a conductive cardiac patch with auxetic geometry was conducted by Olvera et al. [14], who employed MEW to fabricate missing rib geometries using PCL. To impart electrical conductivity, a polypyrrole (PPy) coating was applied to the PCL scaffolds via in situ chemical oxidative polymerisation. Tensile testing revealed that the auxetic patches exhibited a characteristic J-shaped stress–strain curve, with the three previously mentioned phases typical of soft biological tissues [49]. In addition to their mechanical performance, the patches demonstrated conductivity values comparable to those of native myocardium and were shown to be cytocompatible in vitro when cultured with human mesenchymal stromal cells (MSCs).

Brazhkina et al. [3] reported a 3D-printed patch composed of a polycaprolactone (PCL) substrate and gelatin methacrylate (GelMA), designed to support human iCMs. The study compared two auxetic geometries, lozenge truss (in the study referred to as “missing rib”) and re-entrant honeycomb, and found that the lozenge truss exhibited a lower elastic modulus, more closely resembling healthy myocardial tissue. In vitro experiments confirmed the ability of iCMs to adhere, proliferate, and maintain function over a 14-day period.

Finally, Chansoria et al. [12] proposed a rational design framework for auxetic patches targeting dynamic organs such as the heart, lungs, stomach, and bladder. Eight geometrical designs were tested with varying parameters, resulting in 116 patches fabricated via digital light projection. Each patch consisted of a bilayer hydrogel: a non-adhesive PEGDA top layer and a cell-adhesive GelMA bottom layer. Mechanical properties, including Poisson's ratio, transverse stiffness, normalised stiffness, and yield strain, were systematically assessed via in silico modelling and compared to those of target organs. For cardiac applications, the re-entrant honeycomb, arrowhead, and sinusoidal ligament geometries were deemed most suitable due to their high stiffness ratios, as anisotropy can be imparted to those architectures by featuring different designs across different dimensions.

2.4 Piezoelectric materials

Piezoelectricity was first discovered by Jacques and Pierre Curie in 1880 during experiments with quartz crystals and Rochelle salt, demonstrating that applying pressure to these materials led to the generation of electrical charges on their surfaces [54]. Piezoelectric behaviour can be classified into the direct effect, in which mechanical energy is converted into electrical energy, and the indirect effect, where electrical energy induces mechanical deformation [41].

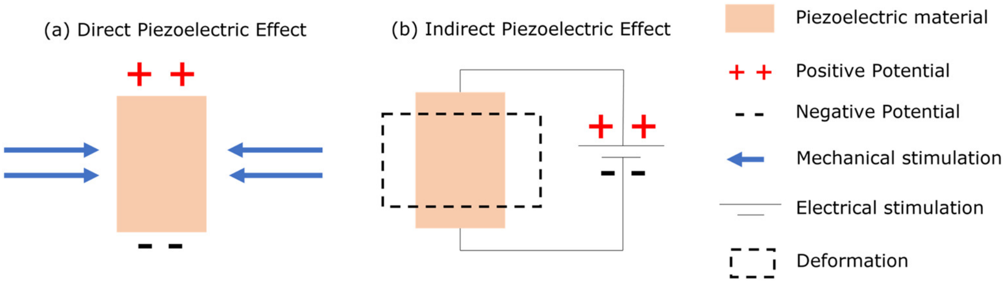

Figure 2.6: Schematic representation of direct (a) and indirect (b) piezoeelectric effect. Taken from [41]

.

The piezoelectric effect occurs in materials that lack a centre of symmetry in their crystalline structure. When an external force is applied, it causes a relative displacement of positive and negative ions within the unit cell, resulting in charge asymmetry and the formation of an electric dipole moment. This dipole formation induces macroscopic polarisation in the crystal, giving rise to a piezoelectric potential in which positive and negative charges accumulate at opposite ends of the material [55] Zhu, 2025 100. The most commonly used coefficient to describe piezoelectric activity is the piezoelectric charge coefficient d_{ij}, defined as:

$$d_{ij} = \left(\frac{\partial D_i}{\partial T_j}\right)_E \tag{2.2}$$

in the context of the direct effect, where D represents the electric displacement due to stress, T the applied stress, and E the electric field strength. Components of d_{ij} for j equal to 1 through 3 are referred to as normal modes, as they couple an electric field to a normal (tensile or compressive) strain and vice versa. Components for j equal to 4 through 6 represent shear modes, corresponding to shear strain in the material [56]. For instance, in the d_{31}mode, the polarisation direction is perpendicular to the direction of applied stress, whereas in the d_{33} mode, they are parallel.

Poling

Poling is a process used to enhance the piezoelectric properties of a material by subjecting it to elevated temperature and a strong electric field [57]. In their natural state, dipoles within a piezoelectric material are randomly oriented, resulting in mutual cancellation and an absence of macroscopic piezoelectricity. When an electric field greater than the saturation field but below the breakdown threshold is applied, the dipoles begin to align in the direction of the field . Heating the material during this process, while keeping the temperature below the Curie point, facilitates dipole mobility and reorientation. To lock this alignment in place, the material is then cooled while the electric field is still applied, establishing a stable polarised structure. [58, 59, 60]

Two widely employed poling techniques are contact poling and corona poling. In contact poling, the material is positioned between two electrodes and subjected to a direct current. Cooling under the applied electric field ensures that the induced dipole orientation is preserved. In contrast, corona poling involves connecting only one side of the sample to an electrode, leaving the opposite surface exposed. A sharply pointed corona electrode, held at high voltage (typically in the kilovolt range), is positioned close to the free surface. The intense electric field at the tip ionises the surrounding gas molecules, which then accelerate and deposit onto the material's surface, inducing polarisation. [60]

2.4.1 Classification of piezoelectric materials

Ceramic piezoelectric materials

Perhaps the most well-known and widely used class of piezoelectric materials, ceramics are renowned for their high piezoelectric performance. They typically possess a perovskite crystal structure and often contain lead, although lead-free alternatives—such as barium titanate (BT) and potassium sodium niobate (KNN)—have been developed to mitigate the hazardous effects associated with lead-based compounds. [61] Ceramics offer several advantages, including excellent piezoelectric properties, low manufacturing costs, simple fabrication techniques, and the ability to be shaped into various geometries. As a result, they are prevalent in applications such as transducers, sensors, and actuators. [61] Among ceramic piezoelectric materials, lead zirconate titanate (PZT) stands out for its exceptional piezoelectric performance, boasting a piezoelectric coefficient of 360 pC $N^{-}1$. Its superior properties, combined with chemical stability and a Curie temperature of 350 °C, have contributed to its widespread adoption since its discovery in the early 1950s. However, PZT also has notable drawbacks, including a high Young's modulus (65 GPa) and density, which render it brittle and incapable of withstanding significant deformation. Moreover, due to the toxic nature of lead, PZT is unsuitable for certain applications, particularly implantable biomedical devices. [61] In general, despite their excellent piezoelectric response, ceramic materials tend to be stiff and brittle, with high Young's modulus values. These characteristics limit their suitability for many tissue engineering applications. [61]

Piezoelectric polymers

In the early 1960s, Kawai et al. [62] discovered that polymers could also exhibit piezoelectric properties. For a polymer to be piezoelectric, it must contain molecular dipoles within its structure. Semi-crystalline polymers, such as polyvinylidene fluoride (PVDF) and its copolymers, consist of small ferroelectric crystallites embedded within an amorphous matrix. When subjected to poling, the dipoles in these crystallites reorient and align, imparting piezoelectric behaviour to the material. Amorphous polymers also contain dipoles, but lack long-range order, and do not reach thermal equilibrium after poling. Instead, their dipoles are frozen in a quasi-stable state. [61] PVDF has been particularly well studied since its discovery in 1969. It is a semi-crystalline polymer composed of aligned molecular chains forming dipoles within the crystalline regions, surrounded by an amorphous matrix. Poled PVDF exhibits a piezoelectric coefficient in the range of −24 to 34 pC $N^{-}1$. PVDF can exist in several phases, among which the α and β phases are the most common. The α phase, formed upon cooling from the melt, is the most thermodynamically stable but non-polar, as alternating fluorine and hydrogen atoms on the carbon backbone result in no net dipole moment. In contrast, the β phase is polar due to the fluorine and hydrogen atoms occupying opposite sides of the chain, resulting in a net dipole moment. Achieving the β phase requires a high degree of crystallinity, typically induced via poling. This transition is further facilitated by the introduction of structural defects, which enhance the piezoelectric properties of PVDF. Common copolymers of PVDF include PVDF-HFP (containing hexafluoropropylene) and PVDF-TrFE (poly(vinylidene fluoride-trifluoroethylene)). These copolymers tend to be more processable and flexible. [63, 61] Although not typically used in energy harvesting due to their lower thermal stability and mechanical durability, piezoelectric polymers are actively explored in tissue engineering. Their flexibility, light weight, and ability to generate sufficient piezoelectric responses for biological stimulation make them suitable candidates. [61, 64, 16, 17]

Biological tissues

The first evidence of piezoelectricity in biological tissues was reported in 1940 by Martin, who recorded electric potentials from a bundle of wool enclosed in shellac and compressed between two brass plates. [65]This phenomenon was later attributed to the inherent polarisation of highly ordered α-helices in α-keratin. [66] Since then, piezoelectricity has been identified in several biological structures, including bone, tendon, skin, and hair. These properties arise from the presence of collagen and keratin—proteins known to exhibit piezoelectric behaviour. [67] While the precise physiological role of piezoelectricity in the human body remains unclear, it has been associated with cellular development and regeneration. [68] In bone, for instance, mechanical stress induces electrical signals known to promote growth, healing, and remodelling. The generated electric potential attracts osteogenic cells through the formation of electric dipoles, which in turn drives mineral deposition—primarily calcium—on the compressed side of the bone. [67] Additionally, both in vitro and in vivo studies have shown that electrical stimulation can enhance osteogenic activity. [69, 70]

Chapter 3

Materials and methods

3.1 Melt electrowriting (MEW)

Melt electrowriting was the elected choice of manufacturing for the patches. The machine used to print was the Spraybase® A-1204-0001-01D (as shown in Figure 3.1), located in the Trinity Biomedical Sciences Institute building in Trinity. The primary polymer employed to print was medical-grade PCL (Corbion PC 12, Mw = 104-125 kg/mol), which has a melting temperature of 60 °C. Piezoelectric polymers also used for printing include PVDF-HFP and a variant of PVDF with high fluidity, a desirable property when working with this process (Kynar 705, supplied by Arkema). To design the printing path needed for the different designs used in

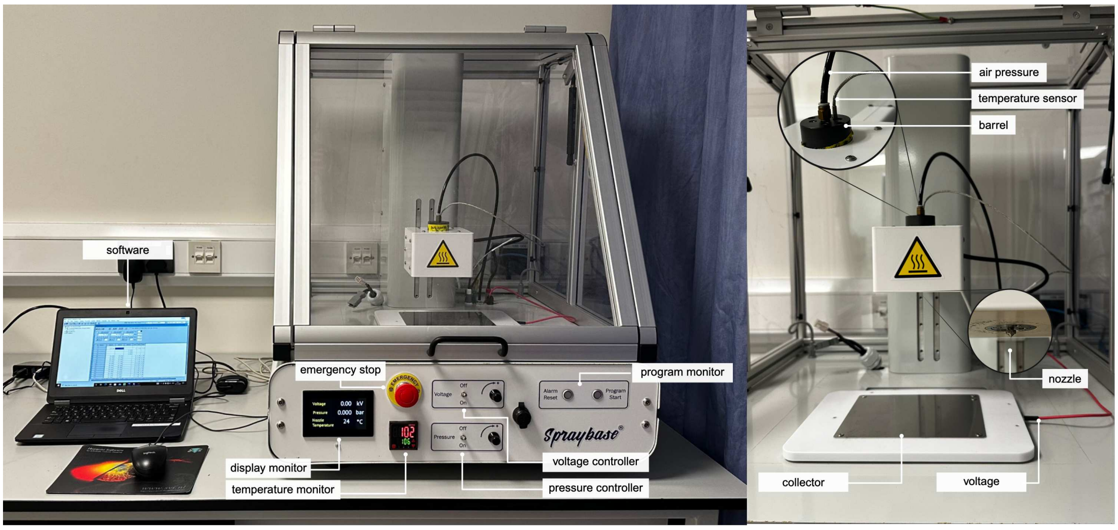

Figure 3.1: Spraybase MEW system

this project, a 2D sketch was first drawn on SolidWorks 2023 and exported as a .dxf file. The sketch was then imported in the software SEL Program Generator (Dispense), which allows to create the "Program" (.m5pg) and "Position" (.m5pt) files that are needed by the MEW machine to print the design. The two files were then loaded on the XSEL software, which is connected to the machine's firmware. The .m5pt file contains, for each line, the start and end position, as well as the speed it needs to be printed. The .m5pg program contains information necessary to communicate with the machine and the sequence in which the lines need to be printed. A schematic representation of the process is shown in Figure 3.2.

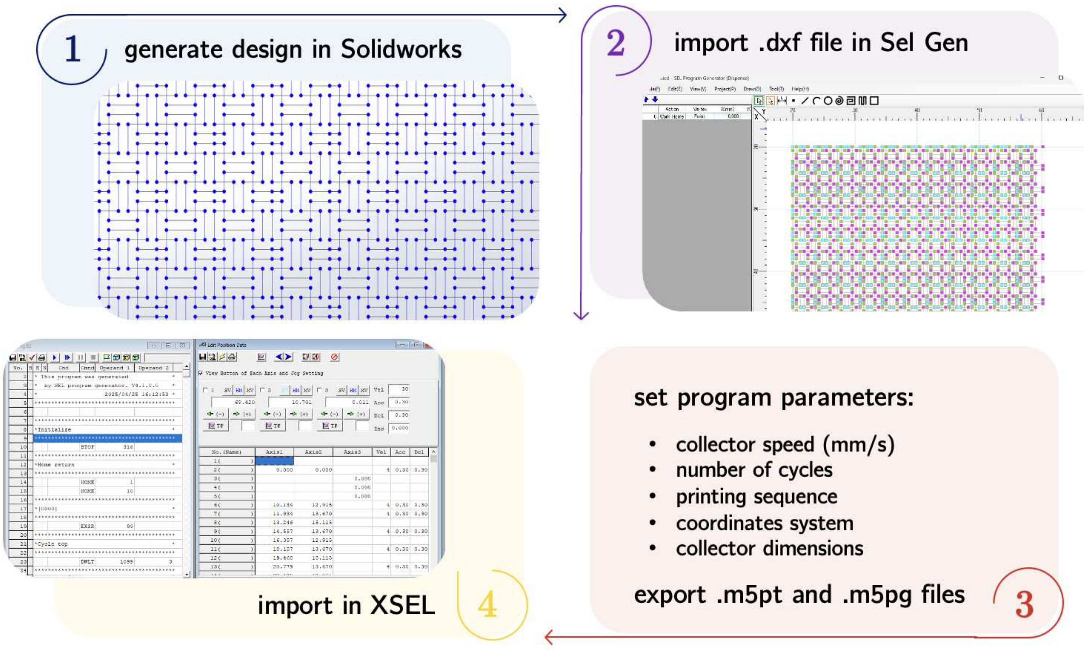

Figure 3.2: Schematic representation of the printing path generation, from Solidworks to XSEL

To prepare for printing, 3 – 5 g of material were loaded into a metallic barrel, which was then connected to a pressurized air supply and a temperature sensor, and mounted in the MEW setup. All printing was conducted using a 0.4 mm nozzle. For each new batch of material, a stabilization period of 60 minutes was observed after reaching the target temperature to ensure complete melting of the pellets. For subsequent prints with the same batch, this period was reduced to 20 minutes. Prior to initiating the printing program, the polymer was extruded onto a peripheral area of the collector plate for approximately 3 minutes, starting from a pressure twice as high as the printing pressure, which was gradually reduced to the target value. This is a common practice when working with MEW [71], as it allows to remove air bubbles during the print and gives time to the jet to stabilize, which in turn yields improved spatial resolution and more consistent prints. Printing was conducted under ambient conditions, with a room temperature of 18 – 22 °C and a relative humidity of 45 - 55%.

3.1.1 Fabrication of PCL patches with lozenge truss design

A series of PCL designs were first fabricated to characterise the influence of geometrical and printing parameters on the mechanical properties of the patches. All samples were printed at a temperature of 105 °C, a pressure of 0.15 bar, and voltages ranging from 7.3 to 7.65 kV. To ensure high printing fidelity, the nozzle-collector distance was kept at 9 mm, and the collector speed was kept at 4 mm/s. Preliminary trials were conducted to identify the smallest feature size that could be reliably fabricated while maintaining structural fidelity. Once these were established, they were defined as the baseline geometry. Using this baseline, a series of patches with a varying number of stacked layers (6, 8, 10, 12, 14) were printed to study the influence of thickness on the mechanical properties. Subsequently, the geometry was isotropically scaled by factors of 1.2 and 1.4, while preserving the aspect ratio and relative proportions of the unit cell, as shown in Figure 3.3. These geometries were printed with 12 stacked layers.

3.1.2 Fabrication of PCL patches with varying auxetic designs

To compare the mechanical properties of varying auxetic architectures, three auxetic designs (lozenge truss, arrowhead and missing rib) were fabricated, along with a standard square grid pattern to serve as control as shown in Figure 3.4. Due to the non-orthogonal nature of the arrowhead design, which deviates from the x-y aligned structure of the other three patterns, fibres tended to misalign at intersection points. To address this issue, the printing path was adjusted to compensate for the phenomenon by slightly deflecting in the opposite direction. Moreover, for this set the nozzle – collector distance was reduced to 6.5 mm, and the applied voltage adjusted accordingly to a lower range of 5.9 – 6.3 kV. The printing temperature, air pressure, nozzle diameter and collector speed were kept constant. All designs were printed with 6 stacked layers, resulting in 12 stacked fibres in the intersection points.

3.2 Solvent casting

For this study, solvent casting was employed to obtain polymer films of PVDF-HFP (Sigma-Aldrich, Mw 400,000) and medical grade PVDF (Kynar 720 MED). Prior to

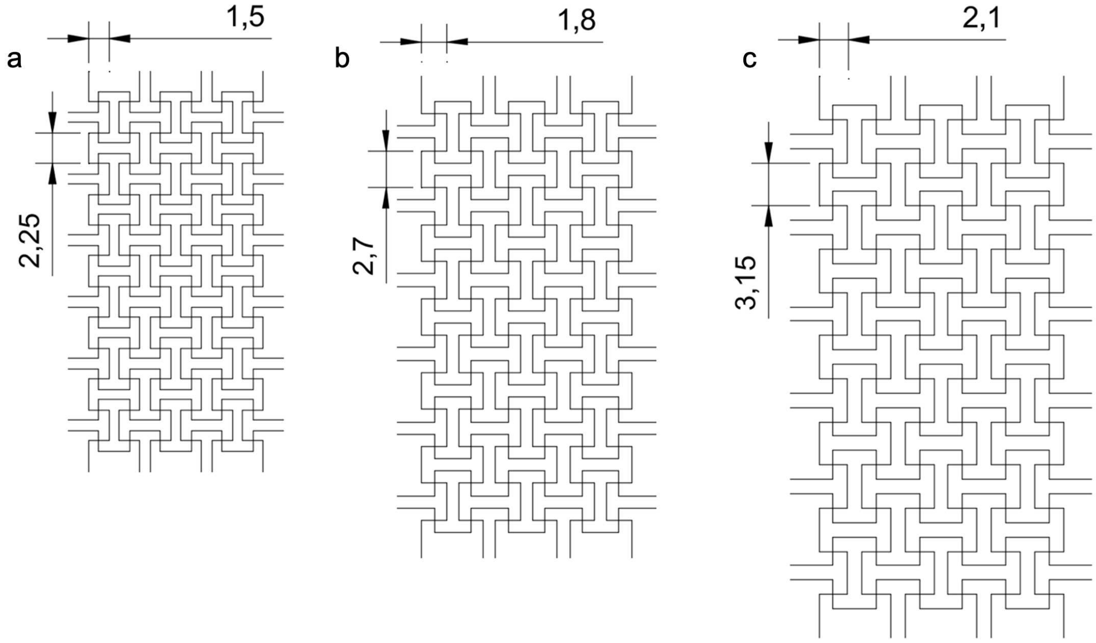

Figure 3.3: Geometric dimensions of the three lozenge truss designs, scaled by factors of 1× (a), 1.2× (b), and 1.4× (c). Key horizontal and vertical unit cell lengths are indicated in millimetres.

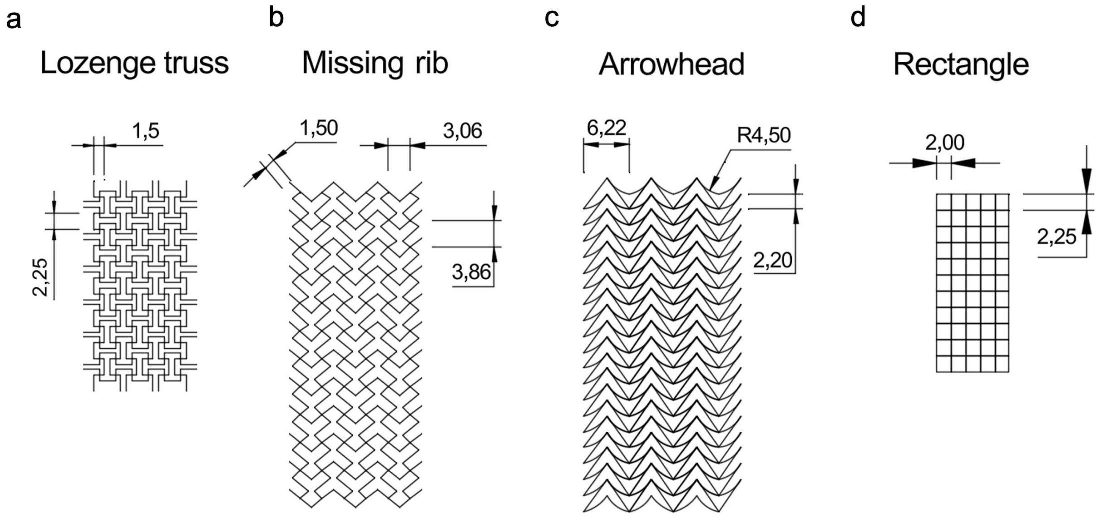

Figure 3.4: Geometric dimensions of the compared designs: lozenge truss (a), missing rib (b), arrowhead (c) and a rectangle grid (d). Key geometrical features are indicated in millimetres.

the solvent casting process, both materials, originally in pellet form, were cryomilled to produce fine powders suitable for dissolution. Cryomilling is mechanical milling process performed at cryogenic temperatures, typically using liquid nitrogen, to grind materials into ultra-fine powders while preventing heat-induced degradation and oxidation. For the procedure, the polymer pellets were placed into a plastic milling tube containing a metal bar (5 mm in length, 9.5 mm in diameter). The tube was then inserted into the cryomilling machine. A pre-cooling phase of 3 minutes was followed by three milling cycles, each lasting 1 minute. For each polymer, 5 % w/v solutions were prepared by dissolving 2 g of polymer in 20 mL of dimethylformamide (DMF). They were then placed under agitation at 90 °C on a hot plate with a magnetic stirrer at 500 rpm for 2 hours, then allowed to cool down for 24 hours. For the solvent casting process, 3 mL of solution were poured into glass Petri dishes and allowed to evaporate overnight.

3.3 Surface treatments

3.3.1 Plasma treatment

Plasma treatment of the patches was carried out using a plasma cleaner (PDC-002-CE, Harrick Plasma). Each patch was placed on a glass petri dish and inserted in the plasma chamber. As the device does not possess a gas inlet, a few drops of hydrogen peroxide H_2O_2 were added to the Petri dish to increase the availability of reactive oxygen species within the chamber during treatment. After creating a vacuum in the chamber, plasma treatment was applied for 5 minutes, in high-power mode, corresponding to a power output of 30 W. This procedure was performed to modify the surface properties of the patches and enhance wettability prior to subsequent coating steps.

3.3.2 Dip coating

To coat PCL patches with PVDF-HFP, 4%, 5% and 10% solutions of the polymer were prepared in dimethylformamide (DMF) as described in section 3.2. The solutions were then cooled down for 24 hours before dipping the melt electrowritten patches. As the viscosity of the 10% solution was deemed too high to carry out dip coating effectively, only the 4 and 5 % solutions were used. Following plasma treatment, the patches were first submerged in the solution for 10 seconds, then removed and placed on aluminium foil. To prevent the solution form accumulating in the macropores of the design, which would compromise the auxetic behaviour of the patch, each sample was gently shaken to dislodge excess solution. The patches were then hung vertically and placed inside a vacuum oven for 5 minutes to ensure the evaporation of the DMF. This dipping and drying process was repeated multiple times, depending on a visual assessment of the coating. Specifically, patches coated with 4% solutions were dipped and dried 5 times, while those coated with 5% solutions underwent the same process 4 times.

3.4 Mechanical testing

Uniaxial tensile tests, both monotonic and cyclic, were conducted on a single-column Zwick machine equipped with a 20N load cell (Figure 3.5). To prevent slippage and ensure a homogenous pressure distribution, the clamped ends of the patches tested were covered in tape. All tests were recorded on video to enable the extraction of the Poisson's ratio at different strains. Force – strain curves obtained from the tests were recorded using the testXpert II software and subsequently imported into MATLAB for further analysis.

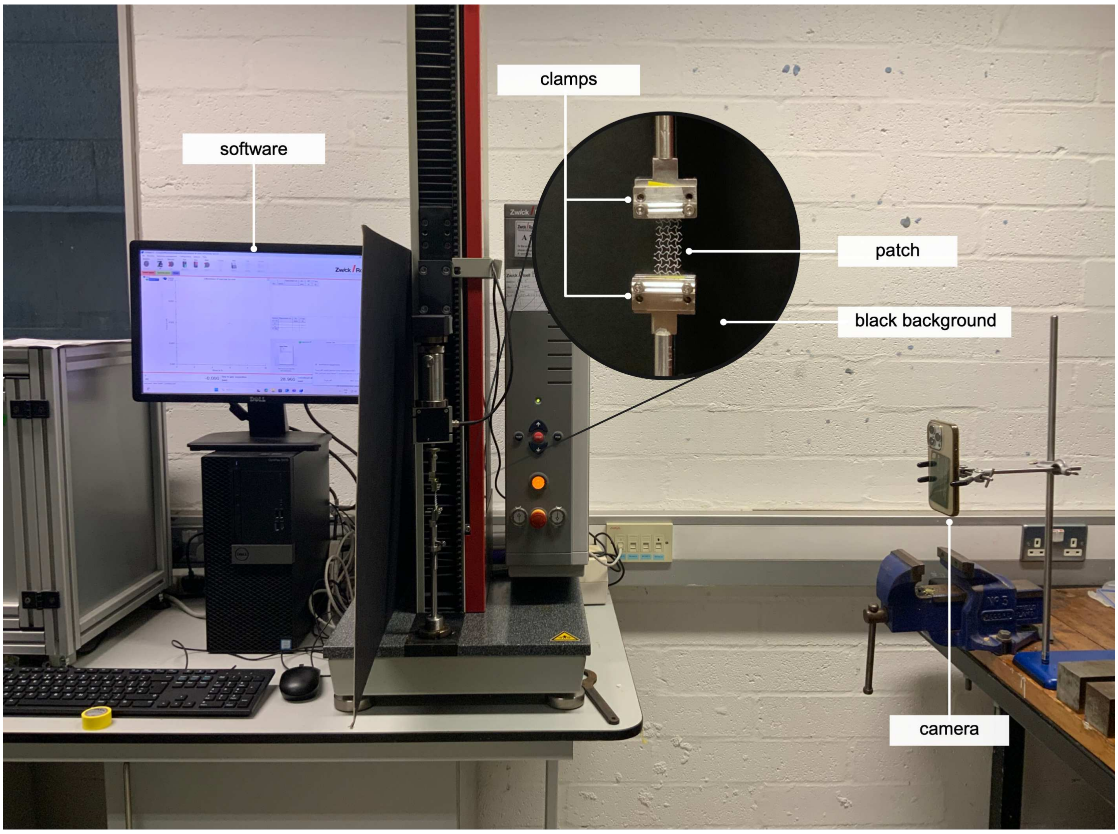

Figure 3.5: Mechanical testing setup

3.4.1 Calculating the stress on the patch

To generate stress- strain curves, the cross-sectional area (CSA) of the patch was calculated using the following equation:

$$CSA = n_L \cdot n_{LF} \cdot A_f \tag{3.1}$$

Where n_L is the number of stacked layers, n_{LF} is the number of longitudinal fibres (i.e., the number of fibres parallel to the loading direction) and A_f is the area of a single fibre. The force data obtained from the tensile test were then divided by the CSA to compute the corresponding stress curves.

3.4.2 Monotonic tensile testing

A pre-load of 0.01 N was applied to each sample for 10 seconds prior to testing. For samples with 1.4 scaling, this value was deemed too high and thus reduced to 0.005 N. The tests were conducted at a rate of 0.1% strain/s until a maximum 80% of strain was reached. As previously discussed, auxetic designs typically exhibit a J-shaped stress–strain curve, characterized by two distinct linear regions. The initial linear region corresponds to the unfolding of the fibers and is therefore strongly influenced by the geometry of the patch. The second linear region, occurring at higher strains, reflects the intrinsic mechanical behavior of the material. In this study, the slope of the first region is referred to as the Toe Region Modulus, while the slope of the second region is termed the Effective Young's Modulus, as neither slope fully aligns with the classical definition of Young's modulus in homogeneous materials. The Toe region modulus of the patches was determined by assuming linear elastic behavior within the initial 5% strain interval. The corresponding stress–strain data was fitted using the polyfit function in MATLAB to perform a linear regression, and the resulting slope was considered the Young's modulus in the Toe region. To compute the Effective Young's modulus, a similar approach was applied to the second linear region of the stress–strain curve. A strain range corresponding to this region was first visually identified, representing the second apparent slope. A 5% strain window was then moved across this region in 1% increments, and for each window, a linear regression model was generated. The R^2 value of each fit was used to assess linearity, and the slope of the model with the highest R^2 was selected as the Effective Young's modulus. The Matlab code used for this processing is shown in Appendix A.

3.4.3 Cyclic tensile testing

Cyclic tests were conducted with the same setup described for the monotonic tensile testing. Testing was conducted at a speed of 0.1% strain/s. Each specimen was subjected to 100 loading–unloading cycles with a maximum strain of 20 %. No conditioning cycles were applied prior to testing. For each cycle, the Toe region modulus was computed similarly as described in Section 3.4.2, limiting the linear region to 1 – 5% strain for more robust calculations. Moreover, the loop hysteresis area was calculated for each cycle, and defined as the difference between the area under the loading curve and the area under the unloading curve. The areas were calculated using the trapz function in MATLAB, as shown in Appendix B.

3.4.4 Custom MATLAB app for data processing

To process mechanical testing data and extrapolate the Poisson's ratio from the mechanical testing videos, a custom MATLAB app was designed, shown in Figure 3.6. After uploading the data obtained from the ZWICK machine and the video of the tensile test, the app enables the user to iteratively scan and select all the intersection points used to calculate the Poisson's ratio at each investigated strain.

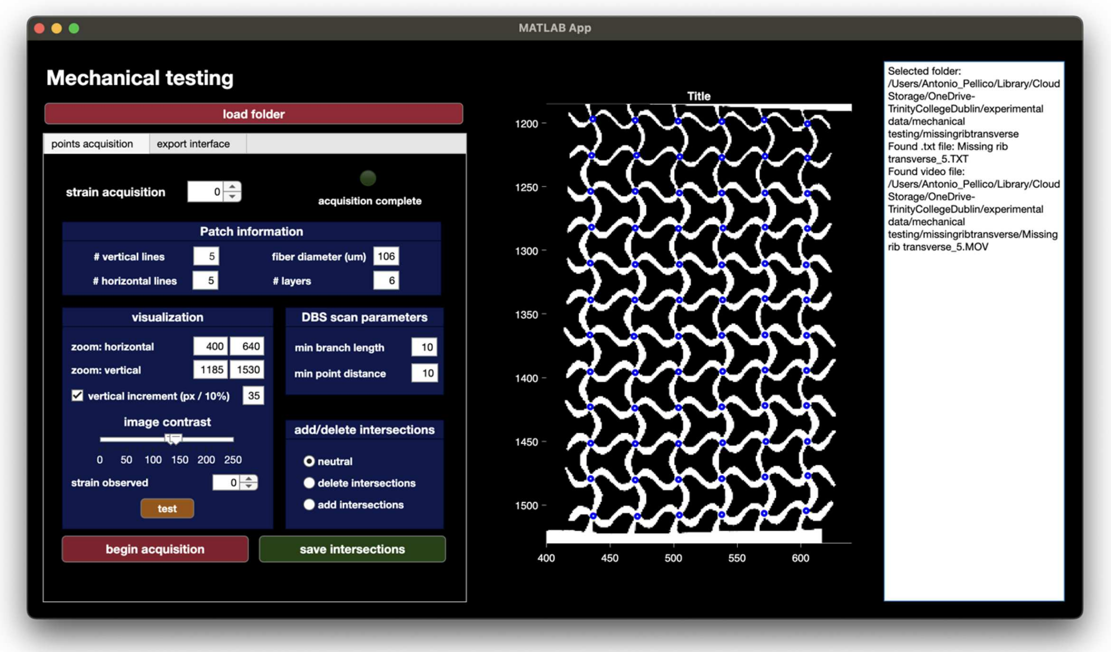

strain acquisition: 0

vertical lines: 5
horizontal lines: 5
fiber diameter (um): 106
layers: 6

zoom: horizontal: 400 640
zoom: vertical: 1185 1530
☑ vertical increment (px / 10%): 35
strain observed: 0

min branch length: 10
min point distance: 10

● neutral
○ delete intersections
○ add intersections

```
Selected folder:
/Users/Antonio_Pellico/Library/Cloud
Storage/OneDrive-
TrinityCollegeDublin/experimental
data/mechanical
testing/missingribtransverse
Found .txt file: Missing rib
transverse_5.TXT
Found video file:
/Users/Antonio_Pellico/Library/Cloud
Storage/OneDrive-
TrinityCollegeDublin/experimental
data/mechanical
testing/missingribtransverse/Missing
rib transverse_5.MOV
```

Figure 3.6: MATLAB app interface

For each strain level of interest, the corresponding video frame is first converted to greyscale. To enhance image clarity and eliminate artifacts, the user can manually adjust the contrast, thus improving mesh-to-background separation. The mesh is then identified as the largest white-pixel object in the image. Since this typically includes both the mesh and the clamps, the user can manually zoom into the region containing only the patch, which is then set as the region of interest (ROI) to exclude the clamps. Subsequently, the ROI undergoes skeletonization, a commonly used image processing technique that reduces the dimensionality of an object to its medial axis (the “skeleton”) [72], essentially reducing the image of the patch to a one pixel wide outline, preserving the shape topology. The skeleton is then used to identify putative intersection points, defined as pixels with 3 or more neighbouring pixels. These candidate points are then clustered using the DBSCAN (Density-Based Spatial Clustering of Applications with Noise) algorithm. DBSCAN identifies clusters based on local point density, allowing for the detection of arbitrarily shaped clusters and exclusion of outliers. It defines clusters as groups of core points, meaning those with a minimum number of neighbours within a given radius, along with all directly density-reachable points. This approach allows DBSCAN to effectively discover clusters of arbitrary shape and to identify outliers as noise without requiring the number of clusters to be specified in advance. As inputs, the algorithm requires the neighbourhood radius, which defines the maximum distance between two points for them to be considered as neighbours, and the minimum number of points required within the neighbourhood for a point to be classified as a core point [73]. In the app, both parameters can be tuned independently for each strain to optimize clustering results. For each resulting cluster, the centroid is selected as the representative intersection point. The app displays all detected intersection points to the user, who can manually add or remove points as needed. Once all intersection points are selected for each strain, the app computes the Poisson’s ratio for each intersection point, by pairing each point with its counterpart on the opposite side of the patch and calculating their distance for each strain level. The Poisson’s ratio is then defined as:

$$\nu_{AB,\varepsilon} = \frac{l_\varepsilon - l_0}{l_0} \tag{3.2}$$

Where $\nu_{\mathrm{AB},\varepsilon}$ is the Poisson’s ratio of points A and B at the investigated strain, l_ε is the distance between the two points at the strain, and l_0 is the distance between the two points at 0% strain. Upon completion, the app can generate and export the following:

- A .txt file reporting the Poisson’s ratio of the patch for each strain, calculated as the mean of the outermost intersection points in the middle rows of the patch;
- A set of images and a video containing colour maps of the Poisson’s ratios at each strain;
- .txt files of the stress – strain curves derived from the tensile test, where the stress calculated as described in Section 3.2.1.

- The Toe region's modulus of the patch, calculated per Section 3.2.2.

A schematic workflow of the app is presented in Figure 3.7.

3.5 Materials characterization

3.5.1 Differential Scanning Calorimetry (DSC)

DSC is an analytical experimental technique that measures the heat flux $\delta q/\delta t$ to or from a sample specimen as well as enthalpy changes as a function of temperature or time. The apparatus consists of two furnaces with controlled atmosphere and independent temperature controller, heating elements, and individual thermocouples. The sample and the reference sample (usually air) are placed inside small independent crucibles made from a high thermal conductive material [74].

In this study, DSC was used to investigate the thermal properties of PVDF-HFP, particularly to verify its melting temperature. This analysis was prompted by repeated unsuccessful attempts to process the material via melt electrowriting. Due to safety concerns, students at Trinity are not allowed to operate the DSC instrument, so the analysis was carried out by Dr. Manuel Reuther, Senior Experimental Officer in the Chemistry department.

3.5.2 Fourier Transform Infrared Spectroscopy (FTIR)

FTIR is a non-destructive analytical technique, used to characterise and quantify multiple material properties, such as crystalline phases, chemical composition and different polymer chain orientations. When a sample is exposed to infrared light, specific functional groups within the material vibrate at characteristic frequencies, absorbing energy at wavelengths corresponding to their molecular bonds. The resulting spectrum provides a "fingerprint" of the material, allowing identification of functional groups, polymer orientation, and chemical interactions. FTIR is widely used in materials science, biology, and chemistry for qualitative and quantitative analysis, as well as for investigating polymer chain alignment and molecular changes due to processing or environmental conditions. Its non-destructive nature and ability to provide detailed molecular insights make it invaluable for characterizing bioinspired and polymeric materials. [74]

In this study, FTIR was employed to analyse the chemical structure and crystalline phase content of samples containing all three of the examined piezoelectric polymers. These included coated patches, solvent-cast films of PVDF-HFP and PVDF 720 MED, thermally processed samples of Kynar 705, and untreated polymer pellets. The measurements were performed using the FTIR spectrometer in the Chemistry department of Trinity. Prior to each scan, both the metallic plate

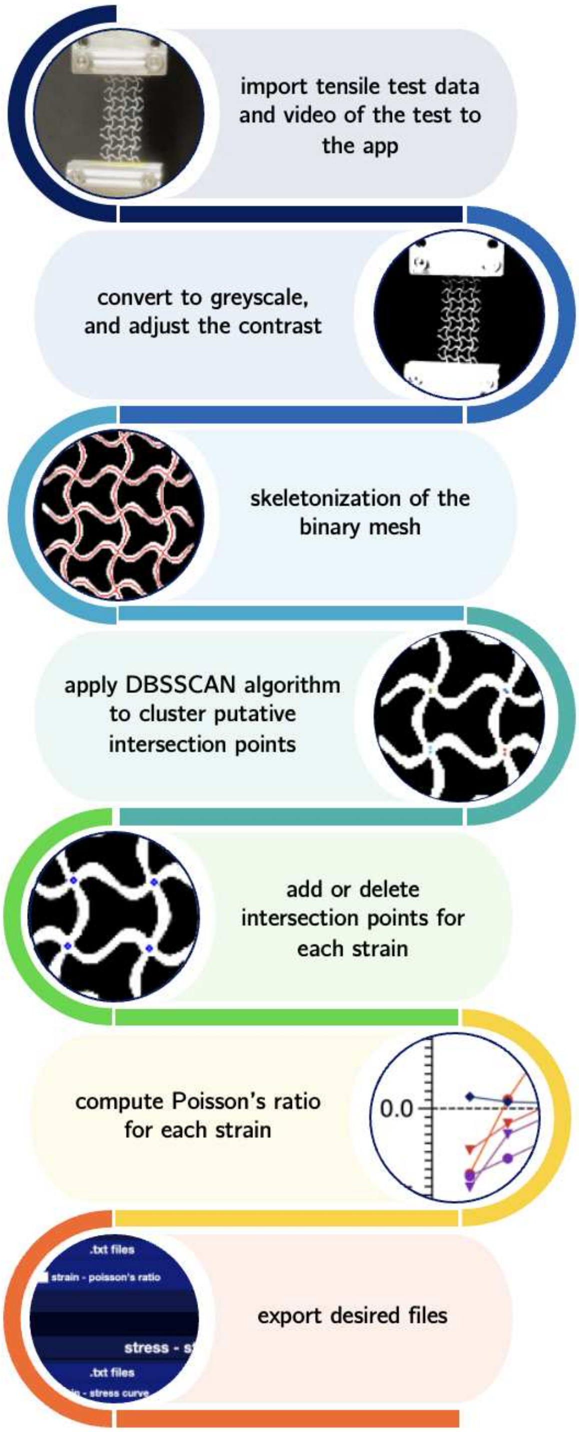

Figure 3.7: Schematic representation of the MATLAB app workflow

and the pressure probe were cleaned with isopropyl alcohol (IPA). A background scan was first conducted without any sample, to remove ambient interference. Subsequently, the sample was placed on the metallic plate, and the probe was tightened to ensure adequate contact. Due to some pre-existing damage to the crystal of the spectrometer, excessive pressure during loading would result in the appearance of some minor peaks in the range of 2300 – 2000 cm^{-1}. As a result, care was taken to control the applied pressure to minimize these effects. The spectral acquisition was performed across a wavenumber range of 4000-600 cm^{-1}, with the output expressed as transmittance percentage. To quantify the β phase content in the samples, a widely known method[75, 76] first described by Cai et al. [77] was used. This approach compares the absorbance intensities of characteristic peaks at 840 cm^{-1} (β- and γ-phase) and 763 cm^{-1} (α-phase) to estimate the relative fraction of electroactive phases (FEA), as shown in Equation 3.3:

$$F_E A = \frac{I_{EA}}{(K_{840*}/K_{763})I_{763} + I_{EA}} \cdot 100\% \tag{3.3}$$

Where $\mathrm{I_{EA}}$ and $\mathrm{I_{763}}$ are the absorbancies at 840* and 763 cm^{-1} respectively; whereas $\mathrm{K_{840*}}$ and $\mathrm{K_{763}}$ are the absorption coefficients at the respective wave numbers, whose values are $7.7 \cdot 10^4$ and $6.1 \cdot 10^4$ cm^2 mol^{-1} . This calculation enabled the comparison of phase composition across differently treated samples to evaluate the effectiveness of coatings and treatments in promoting the formation of electroactive crystalline structures.

3.6 Imaging

Imaging of the patches was performed to qualitatively assess structural features such as fibre stacking and to quantitatively evaluate fibre diameters. Both Scanning Electron Microscopy (SEM) and stereo microscopy were employed for these purposes.

3.6.1 Stereo microscopy

Stereo microscopy was used for initial visual inspection and fibre diameter measurements. Three images per sample were acquired using a stereomicroscope (Leica S6D, Leica Microsystems) at magnifications of 0.8× and 2×. Images were captured with a digital colour camera (Axiocam 208, ZEISS).

3.6.2 Scanning electron microscopy (SEM)

SEM imaging was carried out on three experimental groups, all based on the lozenge truss design: (1) pristine PCL patches, (2) PCL patches dip-coated with a

4% PVDF-HFP solution, and (3) PCL patches dip-coated with a 5% PVDF-HFP solution. Each group was examined under three mechanical states: unstrained, post-monotonic loading at 40% strain, and after 100 cycles of cyclic loading at 20% strain. Prior to imaging, 8mm samples were cut from each patch and mounted using double-sided carbon tapes on aluminium pin stubs. Samples were then sputter coated with a thin gold layer to enhance conductivity. SEM imaging was conducted by Dr. Megan Caravan, at the Centre for Research on Adaptive Nanostructures and Nanodevices (CRANN). Imaging was performed under high vacuum at accelerating voltages ranging from 5 to 10 kV. Images were acquired at both 90° (for fibre diameter analysis) and 45° (to visualize fibre stacking and coating morphology).

3.6.3 Image processing

Fibre diameter measurements were performed using the image analysis software Fiji. For stereo microscopy, three images were analysed per sample at 2× magnification. In each image, three separate fibres were measured, resulting in a total of nine measurements per sample. For SEM analysis, fibre diameter measurements were limited to unstrained PCL patches imaged at 90°, to avoid angular distortion inherent in tilted imaging. Three images per sample were used, with three measurements per image, again yielding nine measurements per sample. All measurements were calibrated using the scale bars embedded in the acquired images. Since the results from stereo and SEM imaging were consistent, optical microscopy was preferred for the majority of the measurements due to its simplicity, reduced cost, and time efficiency.

3.7 Cellular assays

The MTT assay is a widely used colorimetric method for evaluating cell viability, proliferation, and cytotoxicity. It relies on the mitochondrial reduction of the yellow tetrazolium salt MTT to an insoluble purple formazan product by metabolically active cells. Following solubilization in an organic solvent, the amount of formazan can be quantified spectrophotometrically at 570 nm, providing a measure of viable cells [78].

In this study, the assay was used to assess the cytocompatibility of two promising materials, PVDF-HFP and Kynar 705. Primary human macrophages and iPSC-derived cardiac fibroblasts were used as cell models.

Primary human macrophages were differentiated from CD14+ monocytes, as explained in [79]. Briefly, monocytes were extracted form buffy coats, obtained from St. James Hospital in Dublin, under the ethics . The monocytes were then differentiated through addition of 50 ng/ml monocyte-colony stimulating factor

(M-CSF) over a 6 day culture period in RPMI 1640 media, supplemented with 10% fetal bovine serum (FBS) and 2% penicillin/streptomycin (P/S).

SFCi55 iPSCs were used to derive cardiac fibroblasts (iCFs), using a previously established protocol [80]. The initiation of the differentiation was triggered with mesoderm induction on day 0 using 10 µM CHIR99021. Before 72 hours of mesoderm induction, cells were treated with complete FibroGROTM media (Sigma-Aldrich) with 75 ng/ml FGF2 (Biotechne). Cells were kept in culture for 20 days and passaged to cell culture treated flasks (T75) or well plates (6 well plates). Replated iCFs were fed every other day using FibroGRO + 75 ng/ml FGF2 (iCF media).

Both materials were processed to replicate the conditions relevant to their intended application. Specifically, PVDF-HFP was prepared to mimic its use during dip-coating, while Kynar 705 was processed to reflect the conditions typical of melt electrowriting. PVDF-HFP was prepared by solvent casting 5 mL of a 5% (w/v) solution, as described in Section 3.2, while Kynar 705 was thermally treated by melting 4 g of polymer in an oven at 200 °C for 2 hours to replicate the processing conditions used in melt electrowriting. Rectangular samples of comparable size (2 g) were cut and sterilized by immersion in 70% ethanol for 1 hour, followed by a PBS wash.

Conditioned media were prepared by incubating the sterilized material samples in cell-specific media inside 15 mL Falcon tubes at 37 °C under continuous rotation for 48 hours.

Fibroblasts were seeded in 24-well plates at a density of 20,000 cells/well in 400 ţL of medium, 24 hours before treatment with conditioned media. Macrophages were plated plated at a density of 400,000 cells/well one week before performing the assay, as according to the protocol used on that day they reach full maturation. The original media for both cell types was then replaced with 600 μL of conditioned media, and the cells were incubated for an additional 24 hours.

One hour prior to performing the MTT assay, DMSO was added to selected wells to serve as a negative control, for 100% cytotoxicity. For the positive control (100% viability), a separate column of wells containing untreated cells cultured in fresh medium (without conditioned media) was included.

To prepare the MTT working solution, a 5 mg/mL MTT stock in PBS was diluted 1:5 in fresh culture medium. The supernatant in each well was carefully removed, and 600 μL of the working solution was added. After a 4-hour incubation at 37 °C, the solution was discarded, and 600 μL of DMSO was added to dissolve the formazan crystals. The plates were then shaken at 80–100 RPM for 15 minutes at room temperature. 100 muL aliquots from each well were transferred to a flat-bottom 96-well plate, and absorbance was measured at 570 nm. Background absorbance from blank wells (media only, no cells) was subtracted from all values.

All procedures involving MTT powder were carried out under low-light conditions to prevent photodegradation. Each experimental condition was tested in triplicate for macrophages and in four technical replicates for fibroblasts.

Chapter 4

Results

4.1 Standardising comparison across auxetic designs

As previously discussed, different auxetic designs fabricated via melt electrowriting (MEW) exhibit distinct resolution-limiting features, which define the minimum printable element for each geometry. As a result, when each design is printed at its smallest feasible scale, the resulting unit cell sizes differ between geometries. Therefore, to enable meaningful comparisons between different designs, it was necessary to establish a standardised comparison framework first. Two primary factors were taken into consideration: (1) the effect of the unit cell size on the mechanical properties of the patch, and (2) the influence of the number of stacked layers. As mentioned in Section 3.1.1., these considerations were explored using the lozenge truss design as a model. This design was selected due to its compatibility with the x-y grid structure that facilitates its printing. Moreover, its geometric and mechanical isotropy allowed mechanical testing to be conducted along a single axis while still providing a representative overview of the patch's performance.

4.1.1 MEW fabrication of scaled and multi-layered lozenge truss designs

All patches were fabricated using MEW with the parameters detailed in Section 3.1.1. These parameters were optimised to minimise typical MEW defects such as fibre bridging and fibre snapping, with the aim of producing structures with high fidelity and minimal artefacts. This approach was intended to ensure that subsequent mechanical characterisation would primarily reflect geometric and process-related effects, rather than artefacts arising from such manufacturing inconsistencies. Consequently, the printed fibres exhibited an average diameter of approximately 97 μm, significantly thicker than the average range reported in literature of 2-50 μm [71], as confirmed by scanning electron microscopy (SEM) and bright-field microscopy (Figure 4.2). A larger fibre diameter was selected for several reasons. Firstly, to minimise the occurrence of common MEW-related printing defects associated with finer fibres, such as fibre bridging [71]. Secondly, using thicker fibres facilitated the optimisation process, as it allowed reliable diameter measurements using bright-field microscopy. In contrast, thinner fibres would have necessitated scanning electron microscopy (SEM) due to the limitations of optical resolution at the lower micron scale. Overall, the printing fidelity achieved with these settings was satisfactory. However, one phenomenon consistently observed was the fibre hysteresis effect [81]: although the G-code is composed of straight line intersecting at 90°, the actual printed filaments tended to form rounded curves. This effect was less pronounced in scaled-up designs, suggesting that increased feature size improves printability, as intuitively expected. This phenomenon is due to jet lag, defined as the distance between the nozzle position and the point at which the jet falls onto the collector [82]. One common strategy to mitigate jet lag involves increasing the applied voltage; however, this approach introduced undesirable artefacts such as fibre skirting and edge irregularities, as shown in Figure 4.1b.

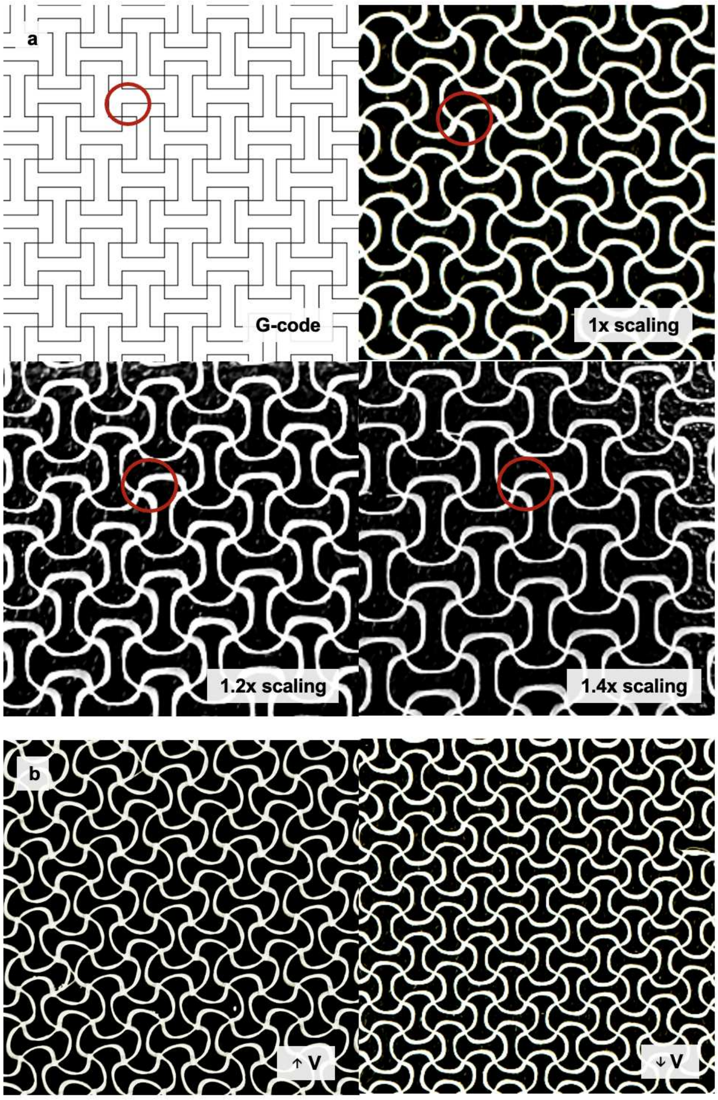

Figure 4.1: MEW results. (a) Comparison between lozenge truss design, and printed patches with 1x, 1.2x and 1.4x scaling. (b) Lozenge truss design printed with higher (7.5 kV) vs lower voltage (6.5 kV).

4.1.2 Imaging and fibre diameter measurement of lozenge truss patches

Imaging of the patches was conducted as described in Section 3.5. A key parameter extracted from the imaging data was fibre diameter, which is critical for the post-processing of mechanical test results, specifically to calculate the CSA. As previously noted, both scanning electron microscopy (SEM) and bright-field microscopy were used to image the samples, as shown in Figure 4.2a and 4.2b. In both cases, the measured fibre diameter was approximately 97 μm (Figure 4.2c). Given the consistency between the two imaging modalities, subsequent fibre diameter measurements were conducted using bright-field microscopy alone, as it provided adequate resolution at significantly lower cost and time.

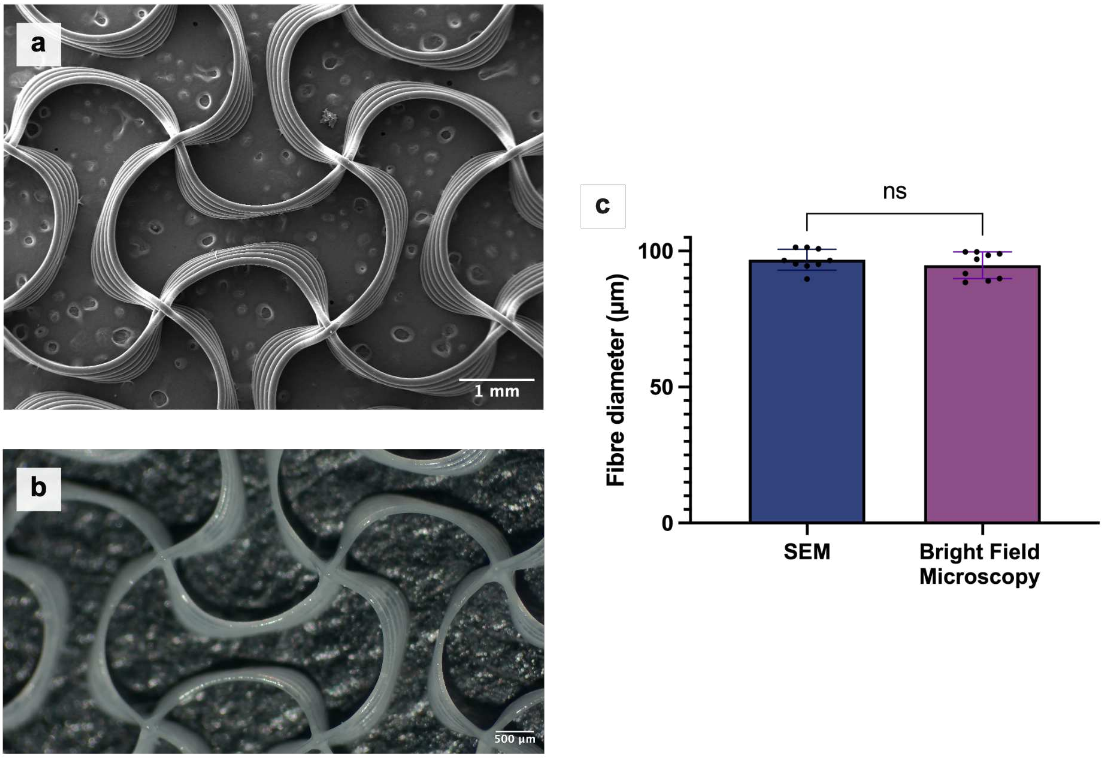

Figure 4.2: Measurements of fibre diameter from SEM and Bright Field Microscopy images. (a). SEM image of PCL patch. (b). Bright field microscopy image, 2x magnification; (c) Comparison of fibre diameter measured from both imaging (N=9). Error bars, mean ± s.d. Unpaired t test ($P < 0.05$).

4.1.3 Monotonic tensile testing of scaled and multi-layered lozenge truss patches

As mentioned in Section 3.4.2, patches were mechanically tested uniaxially up to 80% strain. To assess how the baseline geometry (denoted as 1×) compared to the 1.2× and 1.4× scaled designs, two normalisation strategies were explored. The first maintained a constant number of intersection points across designs, while the second ensured that the physical dimensions of the patches remained constant

(Figure 4.3.). Both approaches offer distinct advantages. The first emphasises the preservation of the intersection points, which are crucial for auxetic behaviour for their role as rotational centres enabling expansion. The second approach is more relevant for translational applications, such as the design of implants for cardiac defects, where it is crucial to understand how different geometries behave mechanically when applied over the same physical area. This comparison aimed to determine whether keeping either parameter constant would allow meaningful comparison of mechanical properties across scaled geometries without introducing significant variation in stiffness.

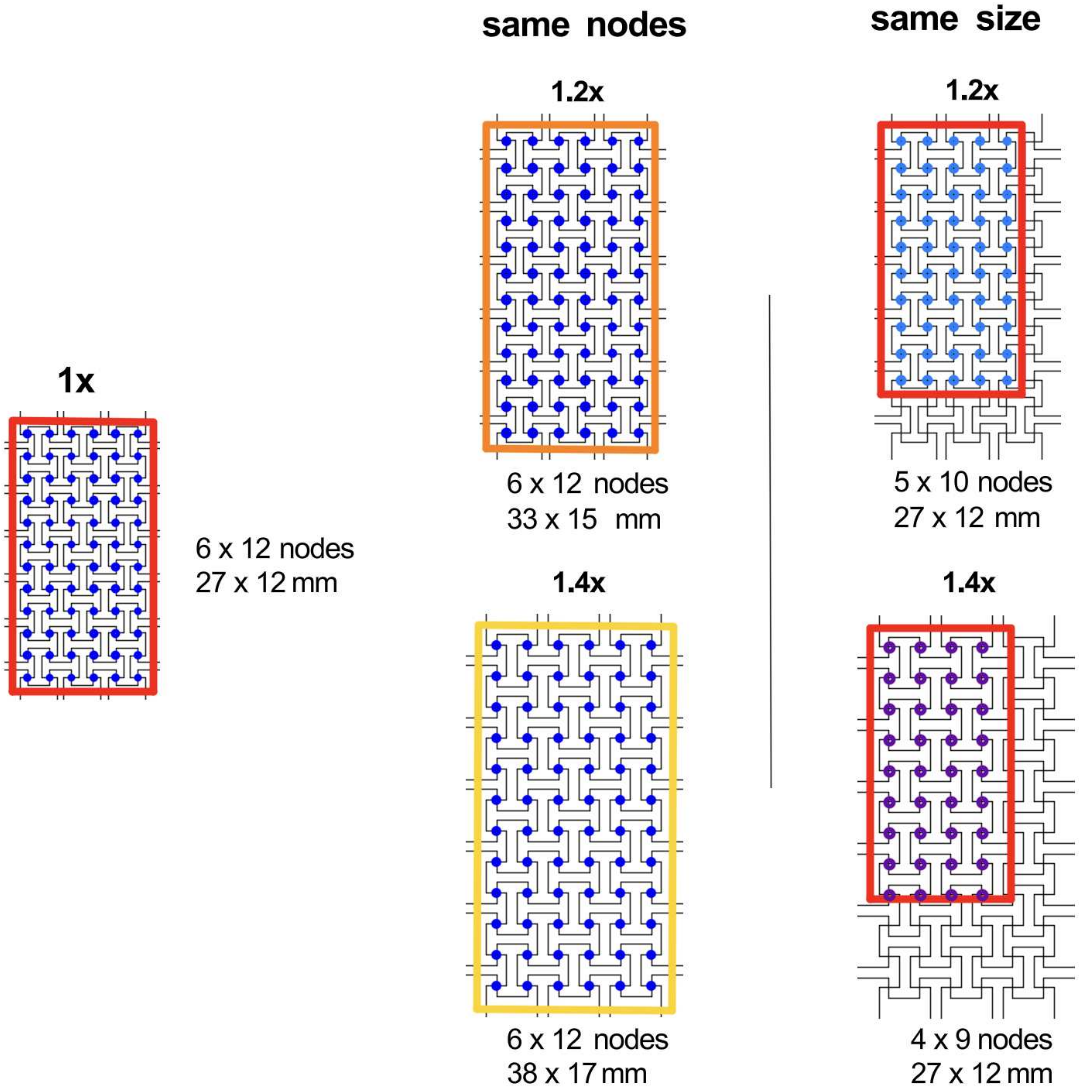

Figure 4.3: Schematic representation of the scaled patches and tested parameters

As shown in Figure 4.4, scaling the geometry significantly affected the Toe Region Modulus (TRM), regardless of whether the patches shared the same dimensions or the same number of intersection points. When normalised by number of nodes, these results aligned with those reported by [12], which found that the TRM is inversely proportional to the square of the scaling factor, as shown in Equation 4.1:

$$TRM_s = TRM_i/s^2 \tag{4.1}$$

Where TRM_s is the Toe region modulus of the scaled patch, TRM_i that of the baseline (1x) and s the scaling ratio. In contrast, scaling had negligible effect on the Effective Young's Modulus, supporting the validity of the CSA estimation method. Since the Effective Young's Modulus is primarily material-dependent, it was expected that geometric scaling alone would not influence it. Only fibres aligned with the tensile direction were considered in the CSA calculation, as these are the principal load-bearing elements at higher strains. This assumption was also validated by the shape of the force-strain curves. When compared across geometries of the same size, normalising by CSA caused the previously distinct curves to overlap, as seen in Figure 4.3, indicating consistent material behaviour. All tested geometries exhibited negative Poisson's ratio values up to 80% strain, as expected. Interestingly, patches tested at the same size demonstrated slightly lower Poisson's ratios. This could be explained by the fact that these patches had lower number of unit cells, meaning that each cell had more space to rotate and unfold, thus augmenting the auxetic effect overall. Instead, patches with the same number of intersection points presented the same Poisson's ratios as the baseline geometry, a result consistent with [12], which found that the Poisson's ratio remained invariant when geometries were scaled while maintaining a fixed number of nodes.

Regarding the number of layers, increasing the layer count predictably increased the Toe region modulus, as shown in figure 4.5. The increase in stiffness at low strains is most likely due to enhanced interlayer interactions. Additional layers introduce more interfacial contacts that resist local deformation, particularly at fibre intersection points. These constraints hinder rotation at the intersection points, which is fundamental to the auxetic behaviour. This interpretation is further supported by the observed increase in Poisson's ratio with the number of layers. The auxetic effect is reduced in thicker constructs because the increased stacking restricts in-plane rotation, which drives the expansion mechanism of the geometry, but is still present in the tested strain range. Notably, this layered constraint does not influence the EYM. This is because the second slope of the force–strain curve corresponds to higher strain regions, where the structure has already unfolded. In this region, the material behaviour dominates the mechanical response, rather than the geometric configuration.

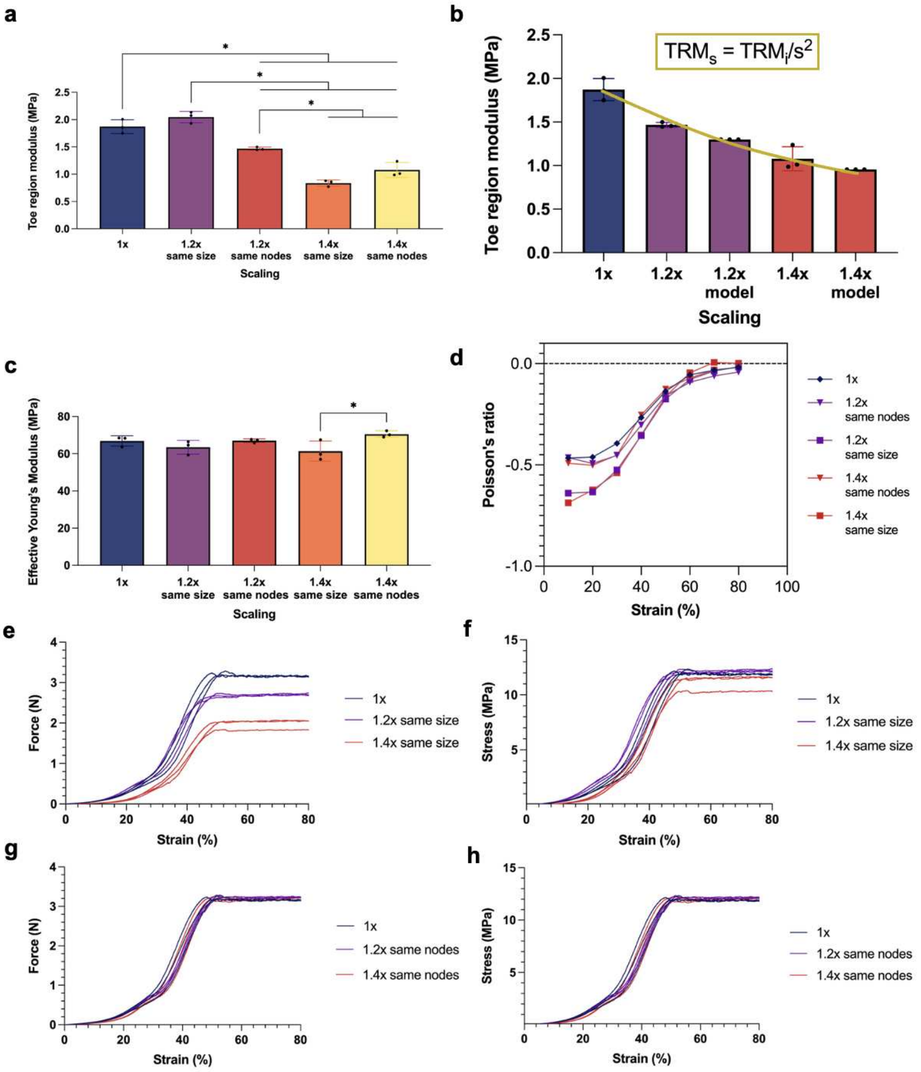

Figure 4.4: Impact of geometry scaling on the mechanical properties of the patch. (a) Toe Region Modulus comparison of scaled geometries. Error bars, mean ± s.d. (b) The Toe Region Modulus of the scaled geometries with the same size is inversely proportional to the square of the scaling factor. Error bars, mean ± s.d. (c) Comparison of the Effective Young's Modulus of scaled patches. Error bars, mean ± s.d. (d) Strain–Poisson's ratio curves of scaled patches, mean only. (e–f) Strain–force and strain–stress curves of patches compared with the same size (N = 3). (g–h) Strain–force and strain–stress curves of patches compared with the same number of nodes (N = 3). (a, c) One-way ANOVA ($p < 0.05$) with Tukey's multiple comparisons tests (N = 3).

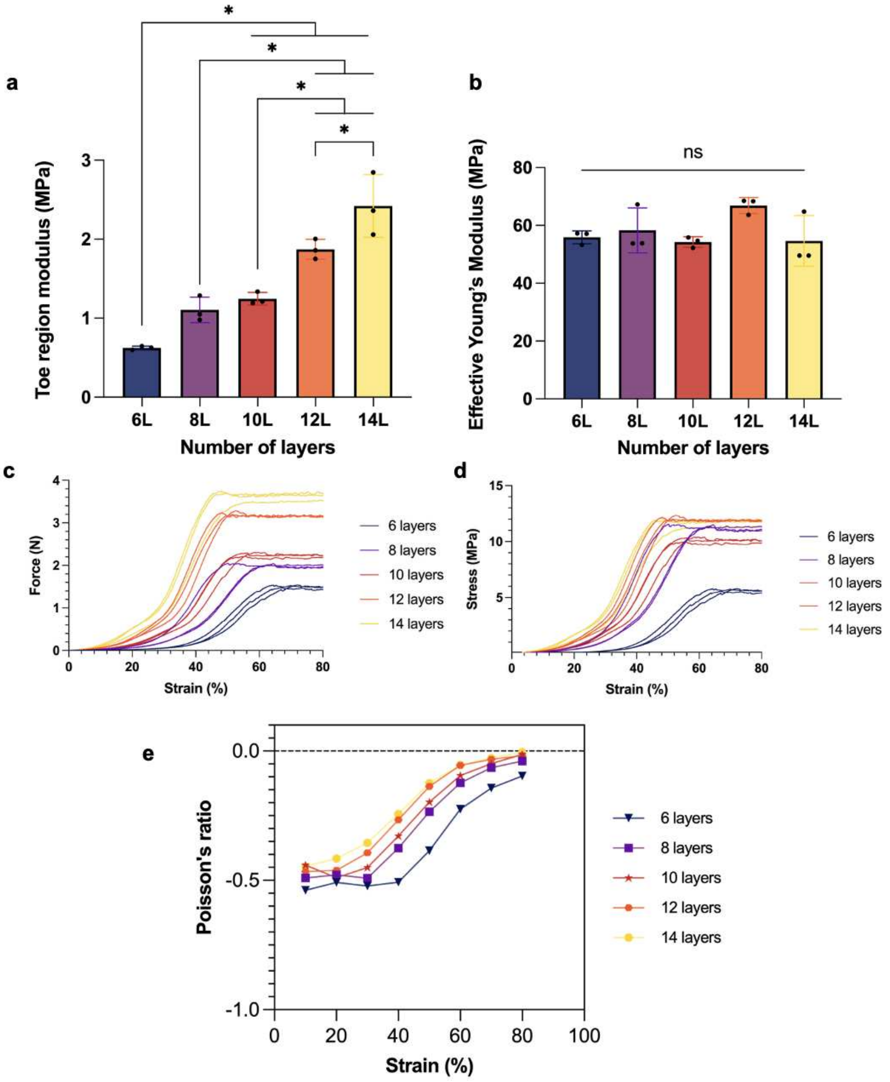

Figure 4.5: Impact of increasing the number of stacked layers on the mechanical properties of the patch. (a) Toe Region Modulus comparison of patches with increasing stacked layer count. Error bars, mean ± s.d. (b) The Effective Young's Modulus remains unaffected by the increase of stacked layers. Error bars, mean ± s.d. (c-d) Strain – force and strain – stress curves of the patches (N=3). (e) Strain – Poisson's ratio curves of the analysed patches (N=3). (a, b) One-way ANOVA ($p < 0.05$) with Tukey's multiple comparisons tests ($N = 3$).

From these results, it was concluded that, while scaling did not significantly affect the Effective Young's Modulus or Poisson's ratio in either experimental condition (constant physical size or constant number of nodes), it did influence one of the key parameters for subsequent analyses: the Toe Region Modulus. This parameter is particularly relevant as it reflects the stiffness of the patch within the strain range relevant to heart motion. Given this, the decision on which parameter to keep constant when comparing geometries was guided by the intended clinical application. As previously discussed, the aim of this study is to develop a patch for implantation onto infarcted myocardial tissue. One of the primary design considerations is therefore to match the stiffness of the patch to that of the infarcted region, in order to provide appropriate mechanical support. As a result, it was deemed more meaningful to compare auxetic designs with the same physical dimensions, as this reflects the actual size of the patch that would be applied to a defined area of fibrotic tissue. Regarding the number of layers, this parameter affected both the Toe Region Modulus and the Poisson's ratio. Based on a balance between mechanical performance, print fidelity, and reproducibility, twelve layers were used as the reference configuration for the remainder of the study.

4.2 Comparison of auxetic designs

As described in Section 3.1.2., a comparative study of different auxetic designs was conducted, comparing the lozenge truss to the missing rib and arrowhead designs. The former was chosen to introduce an anisotropic design, while still maintaining the x-y grid pattern of the lozenge truss for better printability. The arrowhead was chosen to present a design without the x-y grid pattern and with anisotropic behaviour. Moreover, a rectangle grid design was chosen as a negative control.

4.2.1 Melt electrowriting auxetic designs

Preliminary tests conducted on printing the arrowhead with the parameters used in the previous studies with the lozenge truss did not yield positive results, as shown in Figure 4.6a. These patches presented regular defects, where the fibres in the last layers did not follow the curve and the geometry, drawing instead a vertical line to the bottom row. For this reason, new trials using a shorter distance from nozzle to collector were conducted, using the parameters described in Section 3.1.2. Moreover, the G-code was corrected to homogenise the lines curvatures before and after intersection points (Figure 4.6b, circled in blue). This set of parameters provided improved printing fidelity for the arrowhead design. Therefore, it was also used to fabricate the other three designs investigated in this section, to ensure a better comparison. The results were positive for the remaining designs as well, particularly for the missing rib design, which was the second most challenging to print after the arrowhead. (as shown in Figure 4.6c).

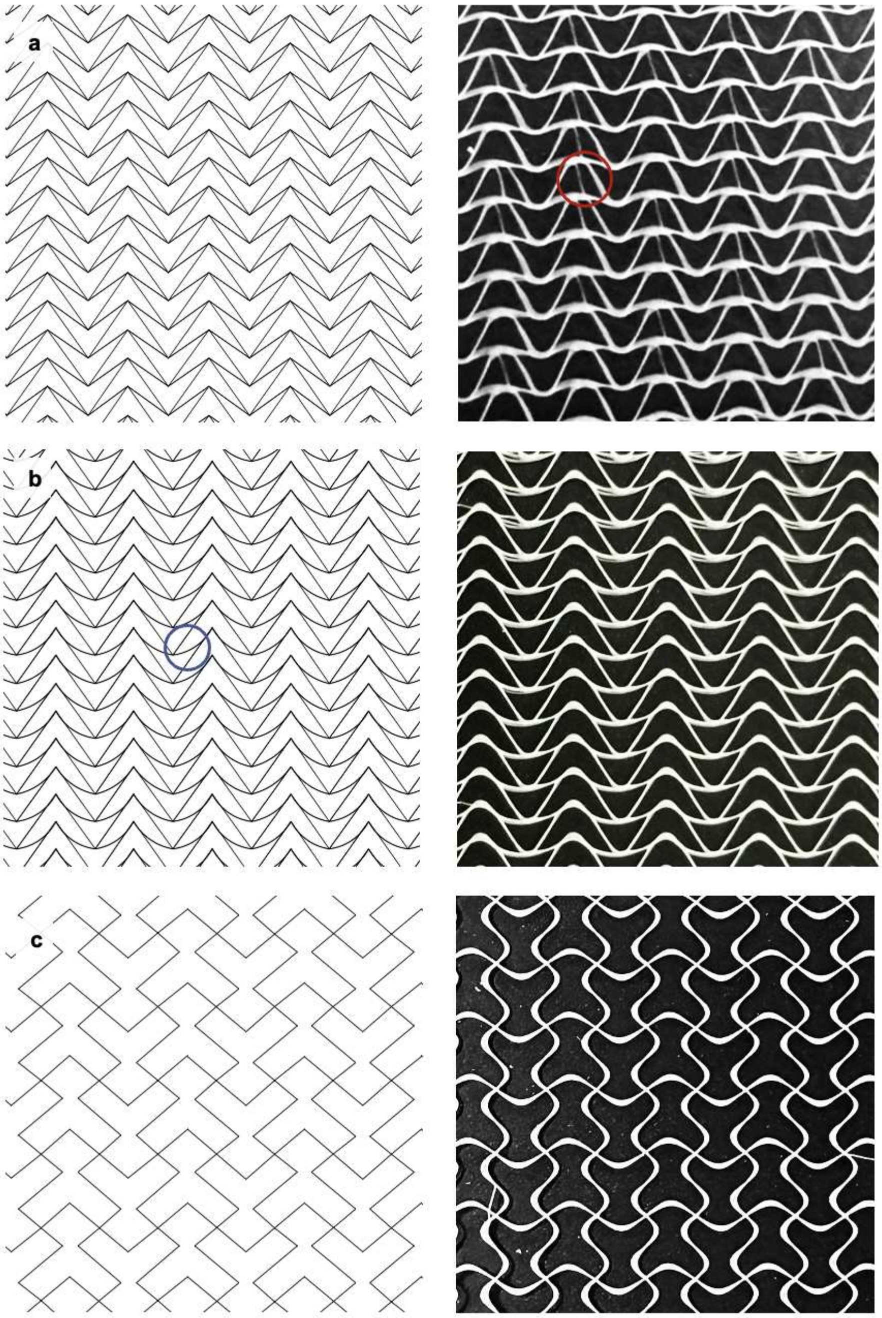

Figure 4.6: Comparison of printing results for auxetic designs. (a) G-code and resulting print of first trial of arrowhead. In red are highlighted the defects. (b) Updated G-code and resulting print of arrowhead with second set of printing parameters. (c) G-code and resulting print of missing rib geometry.

4.2.2 Bright field microscopy of the auxetic designs

As these designs were printed closer to the collector, they exhibited a slightly higher fibre diameter, at 106 μm. As previously discussed, measurements of these diameters were taken only on images captured via bright field microscopy, as shown in figure 4.7.

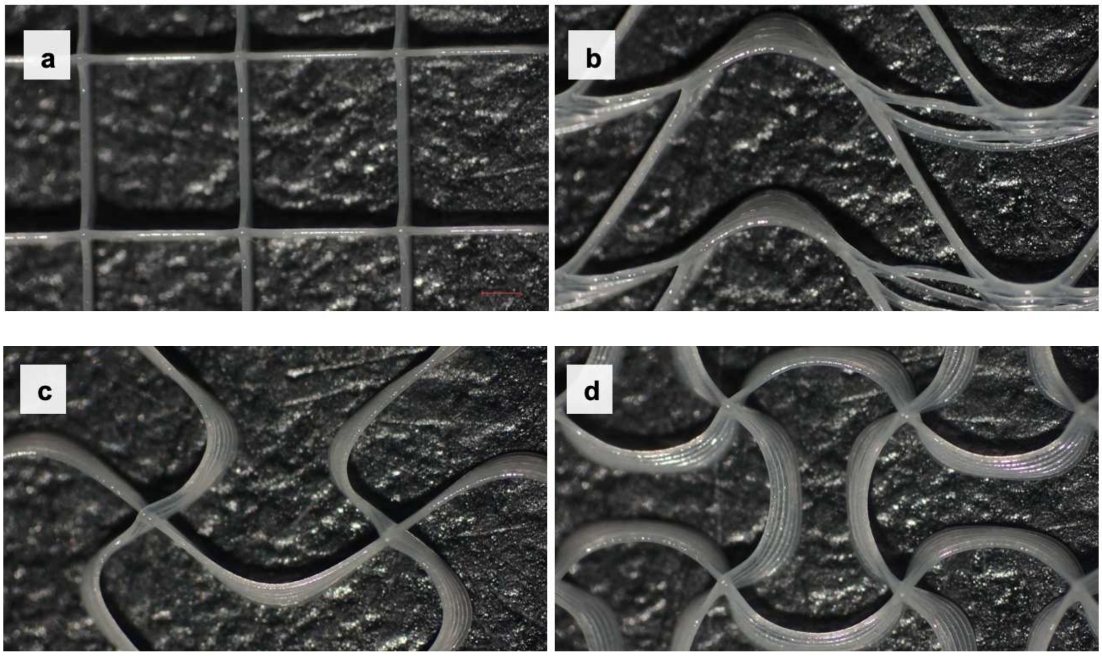

Figure 4.7: Bright field microscopy of auxetic designs, 2x magnification. (a) Rectangle grid d. (b) Arrowhead. (c) Missing rib. (d) Lozenge truss.

4.2.3 Monotonic tensile tests of auxetic designs

Monotonic tensile testing of the patches was conducted as previously described, maintaining the same physical size for all samples, as shown in Figure 4.8. Geometrically anisotropic designs, i.e. arrowhead and missing rib, were tested in both longitudinal and transverse direction.

As shown in Figure 4.9a, all auxetic designs, regardless of whether they were tested in the longitudinal or transverse direction, exhibited a significantly lower Toe Region Modulus compared to the square control, with values over tenfold smaller. No significant differences were observed among the auxetic designs themselves. This, in combination with the comparisons of Effective Young's Modulus and Toe Region Modulus for each design, highlights the substantial impact of geometry on the mechanical properties of the patches, despite identical material composition

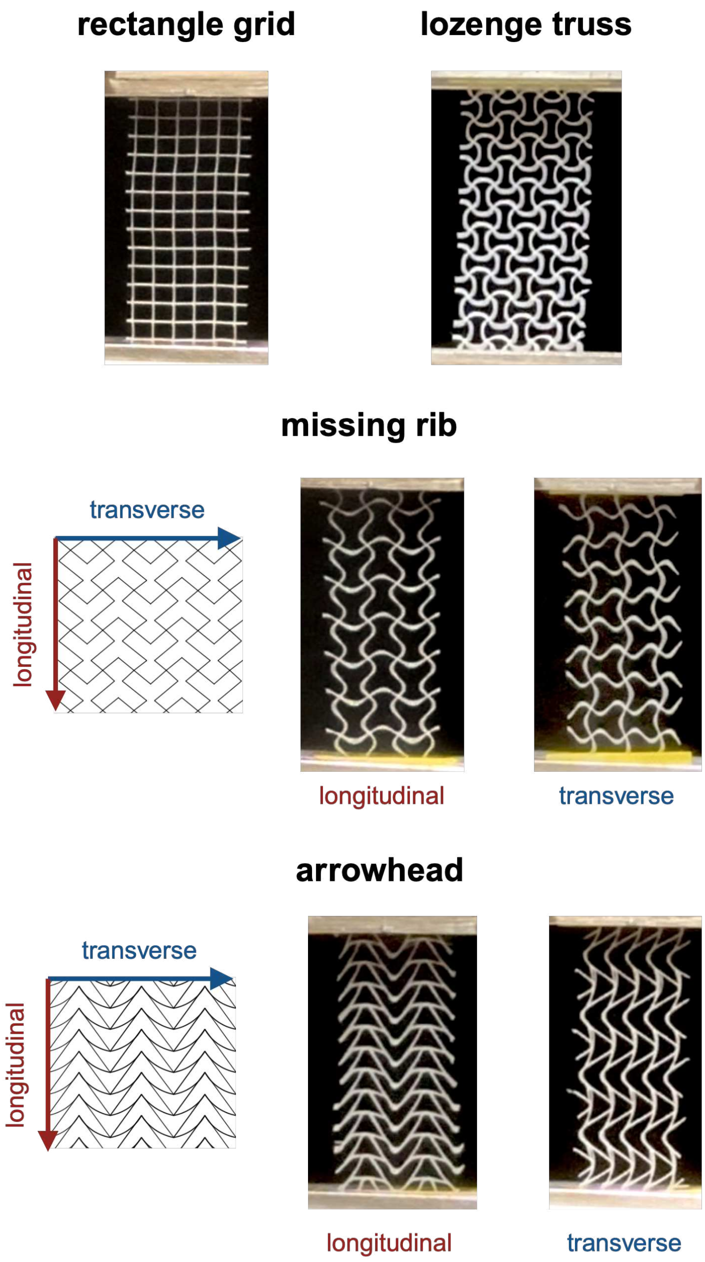

Figure 4.8: Mechanically tested patches, compared with the same physical size.

and processing parameters. Moreover, all auxetic patches, regardless of testing direction, showed the J-shaped stress-strain curves that have been described in Section 2.3.3. Although the optimal stiffness range for cardiac patches remains a matter of ongoing debate, finite element modelling studies suggest that implanting a material stiffer than native cardiac tissue can lead to greater attenuation of wall stress [83]. Experimental data indicate that the stiffness of the left ventricle ranges from approximately 31 kPa at early diastole to between 0.2 and 0.5 MPa at end-diastole. Therefore, a scaffold suitable for myocardial regeneration should ideally exhibit a Young's Modulus within the range of several tens of kilopascals to approximately 1 MPa [32]. While the measured Toe Region Moduli for auxetic designs in the longitudinal direction exceed this range (Table 4.1), it is important to note that these values are tunable. The stiffness can be modulated primarily by reducing fibre diameter and secondarily by adjusting the geometrical parameters of the unit cell. Given that passive myocardial strains reach up to 22% at end-diastole [34], it is also essential that patches remain within their elastic deformation range at these strains. This criterion was met by all patches in the longitudinal direction; however, in the transverse direction, the arrowhead design entered the plastic region at approximately 20% strain. Another important consideration is mechanical anisotropy. The human heart displays an anisotropic stiffness ratio (longitudinal/transverse) ranging from 1.9 to 3.9 [11]. While the arrowhead design exhibits excessive anisotropy, the missing rib design demonstrated a ratio of $E_{trans}/E_{long} = 3.44$, which falls within the physiological range.

Table 4.1: Mechanical properties of auxetic designs

Design	$\mathbf{TRM_{long}}$**(MPa)**	$\mathbf{TRM_{trans}/TRM_{long}}$	$\mathbf{EYM_{long}/TRM_{long}}$
Lozenge truss	4.67 ± 0.7	-	14.31
Missing rib	4.97 ± 1.68	3.44	9.75
Arrowhead	2.06 ± 0.29	14.56	9.57

Analysis of Poisson's ratios revealed positive values for the rectangular grid control, while the lozenge truss and missing rib geometries exhibited negative values throughout the entire strain range considered (Figure 4.10). Notably, both showed their lowest Poisson's ratios within the physiological cardiac strain window. The lozenge truss, in particular, demonstrated a relatively stable Poisson's ratio of approximately –0.5 up to 20% strain. Although values as low as –0.6 to –0.95 have been reported in the literature [12], this study pertains to hydrogels. No prior studies

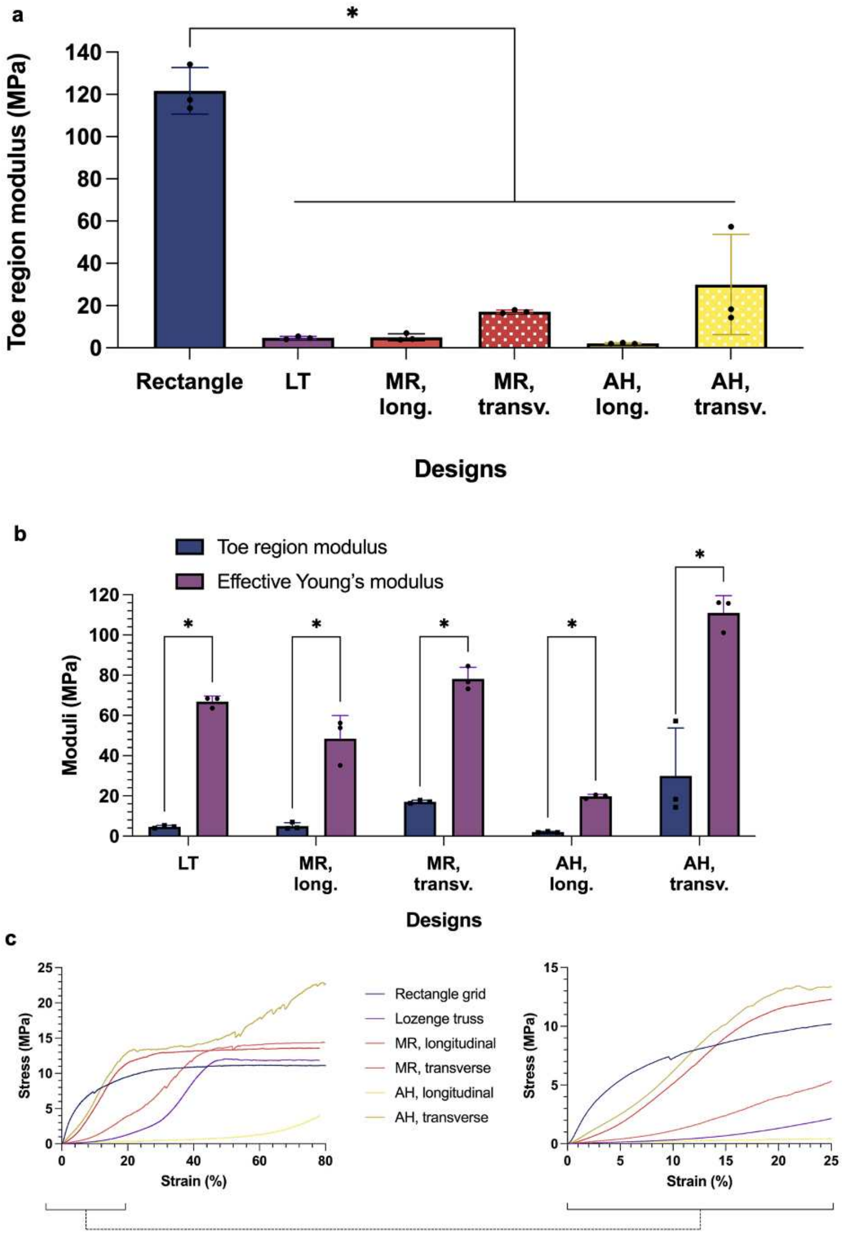

Figure 4.9: Mechanical properties of rectangle grid and auxetic designs. (a) Toe region's moduli. Error bars, mean ± s.d. (b) Comparison of Toe Region's Modulus and Effective Young's Modulus of auxetic designs. Error bars, mean ± s.d. Two-way ANOVA ($p < 0.05$) with Tukey's multiple comparisons tests ($N = 3$). (c) Stress–strain curves; right panel shows stress–strain curves within physiologic strain region. Mean only.

were found using melt electrowriting (MEW) to fabricate this specific geometry. The discrepancy in Poisson's ratio values may be attributable to the differing processing techniques. As discussed previously, the interlayer bonding present in MEW-printed structures can partially constrain rotation at fibre intersections, a key deformation mechanism in auxetic materials, whereas such bonding is absent in hydrogels. This hypothesis is further supported by the Poisson's ratio measured for the arrowhead geometry in the longitudinal direction, which reached –0.4, compared to the –0.7 to 0 range reported by Chansoria et al. [12], depending on geometric parameters. For the missing rib design, Poisson's ratios ranged from –0.45 to –0.15 in the longitudinal direction and from –0.39 to –0.29 transversely. These findings are consistent with those reported by Olvera et al. [14], who studied a MEW-printed missing rib design and observed comparable values not only within the physiological strain range, but also in the overall shape of the Poisson's ratio–strain curves. In both studies, negative Poisson's ratios were observed up to 40% strain in both directions. Although the arrowhead geometry exhibited a Poisson's ratio of –0.4 at 10% strain in the longitudinal direction, this increased to positive values by 20% strain. In the transverse direction, Poisson's ratios ranged from –0.2 to –0.1 within the physiological range. These results suggest that the arrowhead design is unsuitable for replicating the mechanical behaviour of cardiac tissue.

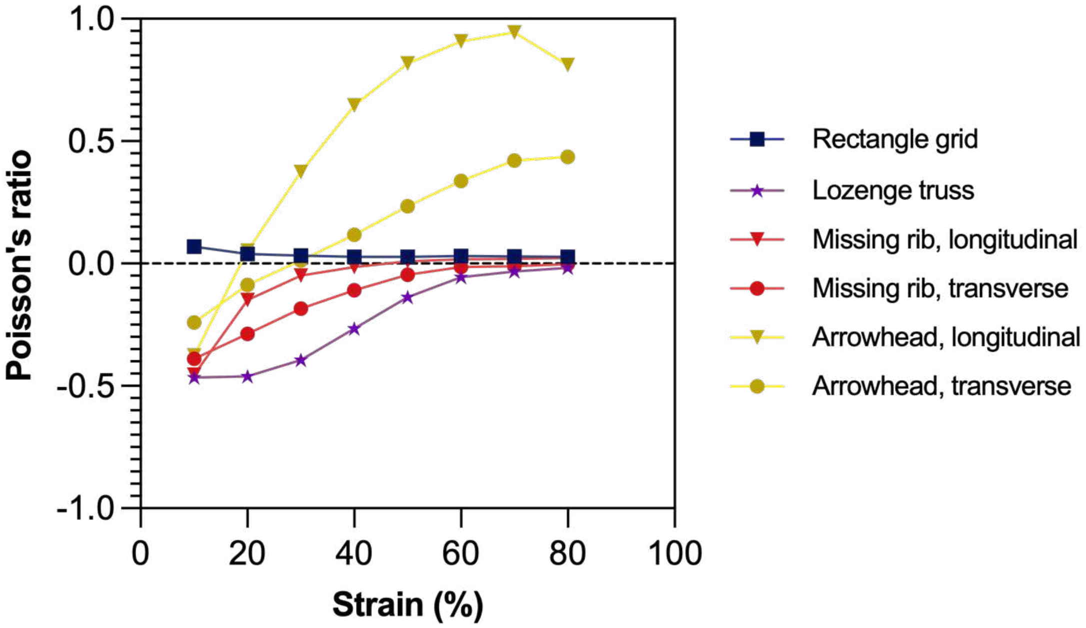

Figure 4.10: Strain - Poisson's ratios curves of auxetic patches. Mean only.

Heat maps of Poisson's ratio (Figure 4.11) further illustrate spatial differences across the patch. In all geometries, Poisson's ratios approached zero near the clamped boundaries, a predictable outcome, as proximity to the clamps inhibits the rotation of intersecting fibres during stretching, and restricts inward deformation at higher strains. This supports the decision to analyse the Poisson's ratio only in the central rows, where deformation is more representative of overall behaviour. Moreover, the deformation patterns differed between designs. In the lozenge truss and arrowhead geometries, lower Poisson's ratios were observed in the central regions, whereas in the missing rib geometry, central values were higher in the longitudinal direction but more uniformly distributed when testing across the transverse axis.

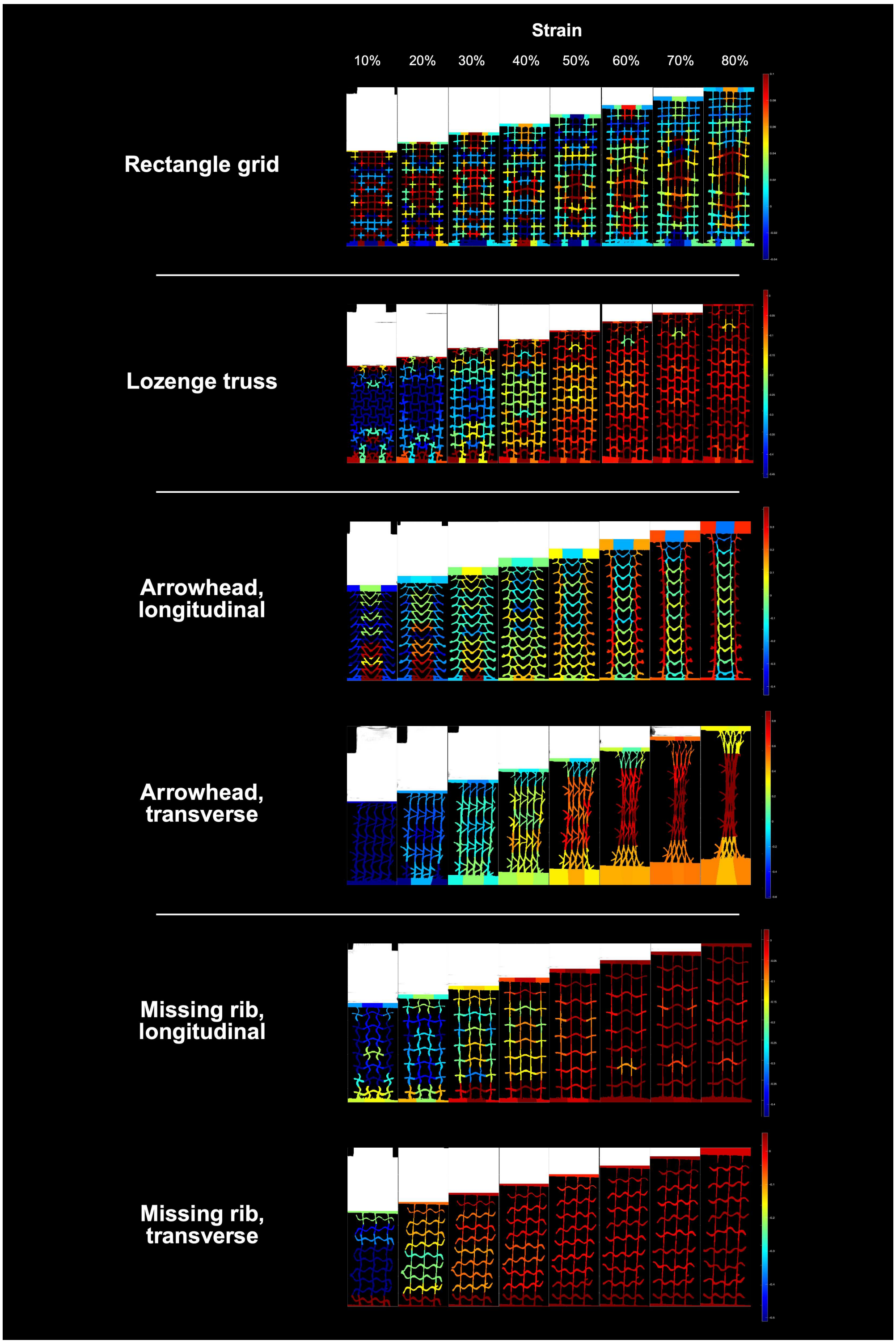

Figure 4.11: Heat maps of Poisson's ratios of auxetic designs

Overall, when evaluating both the stiffness anisotropy (transverse/longitudinal stiffness ratio) and Poisson's ratio, the missing rib geometry emerges as the most promising candidate for cardiac patch applications, as its measured values align more closely with the mechanical requirements reported for cardiac tissue. Specifically, the Poisson's ratio for native cardiac muscle has been reported to fall between –0.2 and –0.5 [12]. While the lozenge truss does possess Poisson's ratio within the desired range, its isotropic geometry limits its suitability for replicating the anisotropic mechanical behaviour of the myocardium. In contrast, the arrowhead geometry, despite its anisotropic features, displayed a stiffness ratio that was excessively high. Furthermore, in the transverse direction, it entered the plastic region within the physiological strain range, which further compromises its suitability for this application.

4.3 Fabrication and characterisation of piezoelectric auxetic patches

4.3.1 Melt electrowriting piezoelectric polymers

As mentioned in Section 3.1, MEW trials were conducted with both PVDF-HFP and Kynar 705. Initial attempts focused on PVDF-HFP, which was selected as an alternative to PVDF due to its lower melting point of 143 °C and enhanced mechanical flexibility [84]. However, despite heating the polymer up to 220 °C, the upper temperature limit of the Spraybase MEW system, no extrusion was achieved. This can likely be explained by the polymer's high melt viscosity, which ranges from 20,000 to 27,000 poise at 230 °C and a shear rate of 100 s^-1, as reported by the manufacturer. Given that the maximum achievable temperature was 10 °C below this benchmark, it is also reasonable to assume that the viscosity remained too high for successful MEW processing. Consequently, PVDF-HFP was deemed unsuitable for further experimentation with MEW. Following attempts on printing with piezoelectric polymers focused on Kynar 705, a polymer in the family of PVDF with high melt flow rate (29.0 - 37.0 g/10 min at 230 °C, as reported by the manufacturer). This polymer has a reported melting temperature of 165–172 °C, thus it was heated to 190 °C and extruded using the same parameters previously optimised for PCL (Section 4.3.1). Although extrusion was achieved, the polymer consistently solidified before reaching the collector, preventing fibre deposition and stacking. This issue, commonly reported in the literature [85], is attributed to the rapid solidification kinetics of melted PVDF when extruded. Numerous following attempts at changing key printing parameters, i.e. voltage, nozzle – collector distance, collector speed and temperature, failed to overcome this limitation. A commonly proposed solution in literature involves the use of a heated collector [85, 86], which reduces the difference in temperature between the barrel and the collector itself, thus preventing premature solidification of the fibres. Xu et al. [87] described the construction of a heated collector using a plastic holder, a silicon heating pad, a glass plate for electrical insulation, and a metallic plate as the collector. However, this solution was implemented, in a custom-built MEW machine, which offered greater flexibility than the Spraybase system, which is essentially a closed loop. Although modification to the Spraybase system has been reported [88] , this involved heating with a hotplate to temperatures to 80 °C, significantly lower than optimal temperature range of 100-120 °C suggested for PVDF processing [89]. Furthermore, the use of a hotplate introduces physical bulk, which may distort the electric field and interfere with stable jet formation. To address this, a custom modification was designed based on Xu et al.'s setup [88]: a silicon heating mat for thermal input, a glass slide for electrical insulation, and the original metallic collector of the Spraybase system. The aim was to minimally alter the commercial setup in order to preserve system integrity while enabling heated collection. Unfortunately, due to time constraints and supplier delays, implementation of this modification could not be completed within the timeframe of this project, thus justifying the shift to dip coating as a technique to introduce piezoelectric properties to auxetic patches.

4.3.2 DSC of PVDF-HFP

DSC analysis was performed following the unsuccessful MEW processing attempts of PVDF-HFP to verify the polymer's melting temperature. As shown in Figure 4.12, the DSC thermogram revealed a melting peak at 117 °C, which is below the maximum temperature reached in the MEW machine (220 °C). Notably, this value is lower than both the manufacturer's reported melting temperature (130 °C) and the range typically cited in the literature (120–140 °C) [63, 90, 84]. While this finding confirms that the polymer does indeed melt well below the MEW system's upper temperature limit, it does not, in itself, explain the failure to process the material. Melting temperature alone is insufficient to determine printability via MEW: the rheological properties, particularly viscosity and viscoelastic behaviour near the melt state, play a critical role. It is possible that, despite reaching its melting point, PVDF-HFP does not achieve the low-viscosity melt flow characteristics required for stable jet formation and fibre deposition, as mentioned in the previous Section. Furthermore, the absence of published studies on MEW processing of PVDF-HFP supports the hypothesis that its rheological profile is incompatible with the technique.

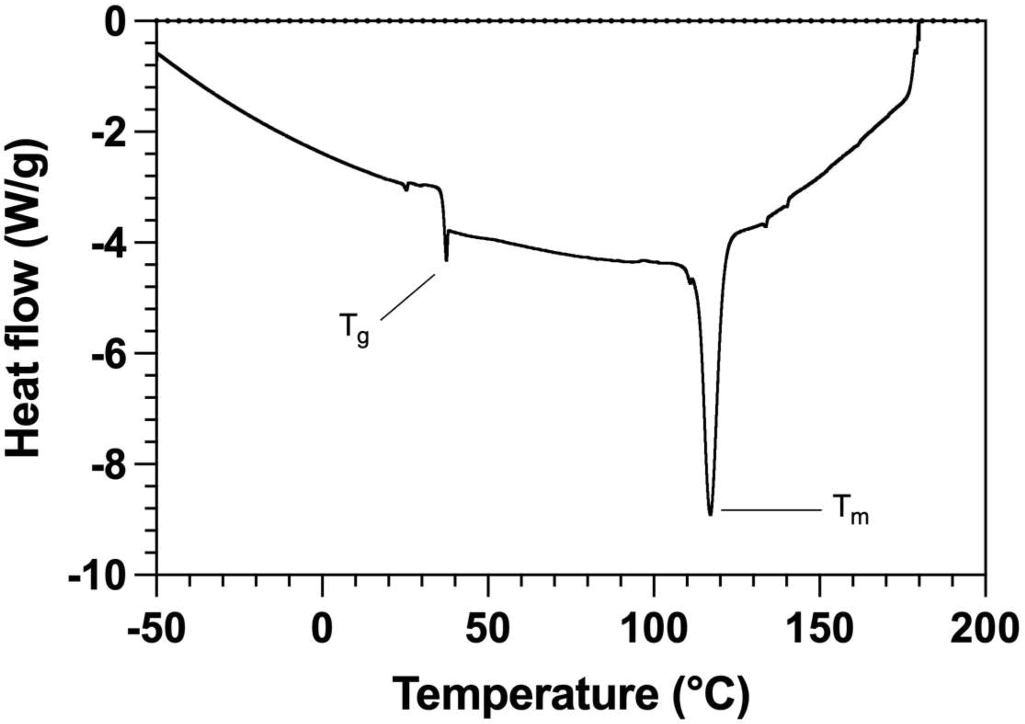

Figure 4.12: DSC analysis of PVDF-HFP.

4.3.3 Solvent casting

To assess the suitability of piezoelectric polymers for the dip coating process, as well as to evaluate their capacity to form continuous films for subsequent characterisation, solvent casting was performed as described in Section 3.2. Kynar 720 MED formed an extremely brittle film, disintegrating into powder upon attempted removal from the Petri dish (Figure 4.13a). This suggests poor film-forming ability and mechanical integrity in the dry state. As a result, the material was deemed unsuitable for dip coating, under the rationale that if a continuous free-standing film could not be formed, it was unlikely to produce a uniform or adherent coating on the PCL patches. Conversely, solvent casting of 5% PVDF-HFP in DMF resulted in a continuous, uniform film after overnight solvent evaporation in a fume hood (Figure 4.13b). Although some wrinkling and shrinkage were observed, the film was readily detached from the Petri dish, indicating good cohesion and flexibility. Based on this performance, PVDF-HFP was selected for further dip coating experiments.

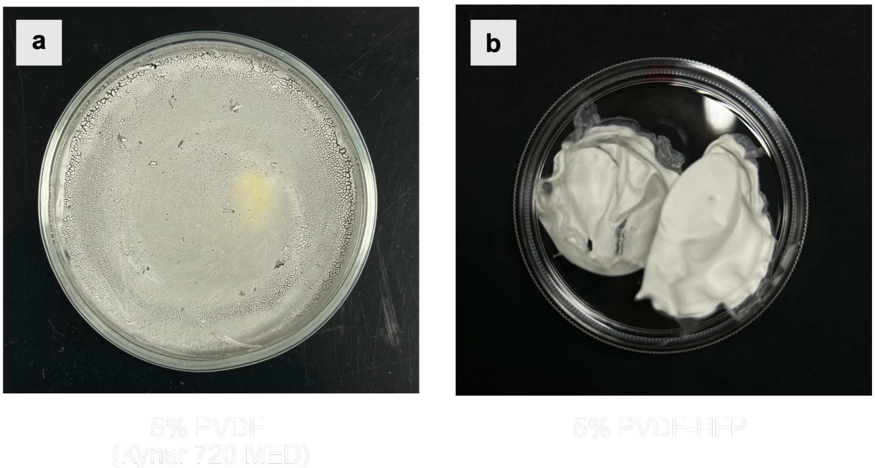

Figure 4.13: Solvent casted piezoelectric polymers. (a) Solvent casted 5% PVDF (Kynar 720 MED). (b) Solvent casted 5% PVDF-HFP.

4.3.4 Dip coating

As described in Section 3.3.2, 4% and 5% (w/v) PVDF-HFP solutions in DMF were used to dip-coat PCL patches with a lozenge truss geometry. Higher polymer concentrations were excluded due to excessive viscosity, which impaired solution infiltration into the porous mesh and resulted in poor coating uniformity. A major challenge was the accumulation of solution between fibres (Figure 4.14). If not fully removed before drying, residual solution would leave a rigid PVDF-HFP film after solvent evaporation that substantially impaired the mesh's ability to deform. To mitigate this, lower concentration solutions were favoured despite their reduced deposition per coating cycle. Instead of increasing solution viscosity, the coating process was repeated multiple times to gradually build up a conformal layer while allowing intermediate drying and solvent removal. This approach prioritised mechanical performance over coating thickness, with the aim of preserving the auxetic behaviour of the scaffold.

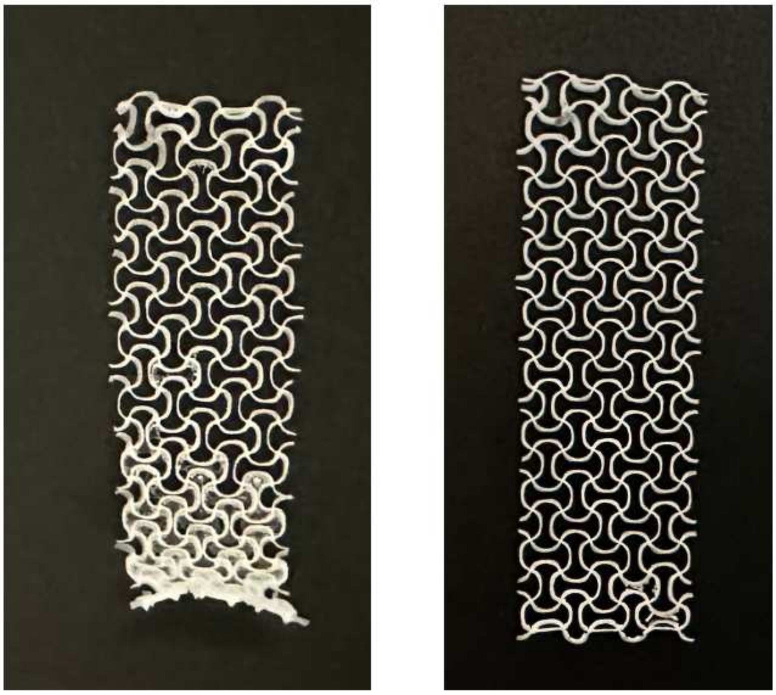

Figure 4.14: Lozenge truss PCL patches dip-coated in 5% PVDF-HFP solution. Left: excess solution not removed prior to drying, resulting in stiff, obstructive PVDF-HFP films between fibres. Right: excess solution properly removed, preserving mesh openness and flexibility.

4.3.5 Monotonic tensile testing of PVDF-HFP coated lozenge truss patches

To assess whether PVDF-HFP coating affects the mechanical performance of PCL patches, samples coated with 4% and 5% PVDF-HFP solutions were tested under uniaxial tension up to 80% strain. As shown in Figure 4.15a, the Toe Region

Modulus of coated patches was slightly higher than that of uncoated ones, though the difference was not significant. This outcome is expected, as the initial stiffness in this region is primarily governed by geometry, which remained unchanged. However, the coating did affect the Effective Young's Modulus (Figure 4.15b), which was lower in coated patches. This reduction may be attributed to residual dimethylformamide (DMF) from the dip-coating process or the plasma treatment, which could have slightly degraded the PCL or reduced adhesion between stacked fibres, both factors that would compromise material stiffness in the later stages of deformation, where response is more material-dependent. This reduced inter-fibre bonding might also explain the higher auxetic response observed in coated samples (Figure 4.15c), which showed consistently lower Poisson's ratios across the entire strain range. Looser fibre junctions could allow greater rotation at intersections, facilitating more pronounced lateral expansion. Overall, while the stress–strain curves of coated and uncoated patches differed (Figure 4.13d), both 4% and 5% PVDF-HFP coatings preserved the auxetic behaviour and did not significantly affect the Toe Region Modulus. The differences between the two concentrations were minimal, so no clear preference emerged. Both were therefore considered suitable for further investigation. There is limited literature on the effect of PVDF-based coatings on the mechanical behaviour of melt electrowritten PCL scaffolds. However, a study by Balzamo et al. [91] investigated electrospun PCL mats brought into contact with a PVDF-DMF solution deposited on an aluminium substrate. After solvent evaporation, microspherulitic PVDF particles were observed on the mat, occasionally bridging adjacent fibres. This resulted in an increase in tensile strength compared to pristine PCL mats, particularly at PVDF concentrations above 16%. At lower concentrations (13%), no clear difference in elastic modulus was reported. However, no statistical analysis was provided, limiting the conclusions that can be drawn. Furthermore, the coatings in the present study differ markedly in microstructure: as shown in Figure 4.17, no spherulitic formations were observed, and no fibre fusion occurred. It is therefore expected that the coating here would have a smaller impact on mechanical properties than reported by Balzamo et al.

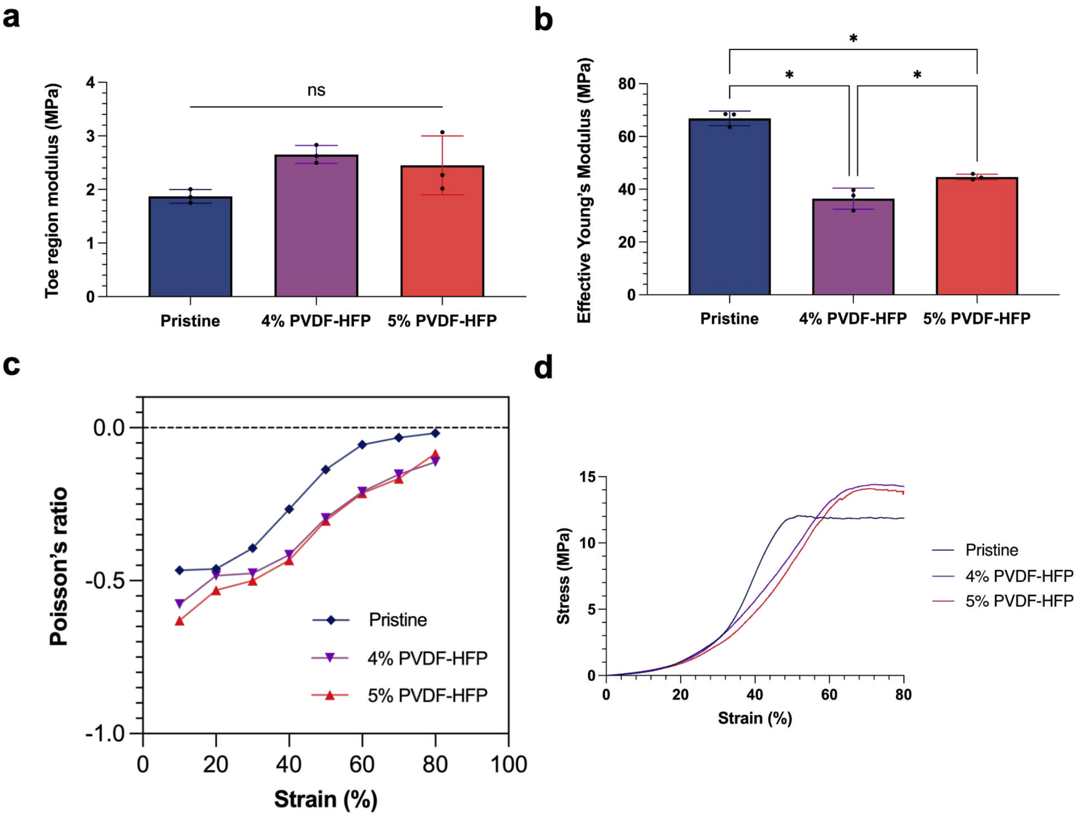

Figure 4.15: Monotonic tensile testing of PVDF-HFP coated patches (a) Toe region modulus. Error bars, mean ± s.d. (b) Effective Young's Modulus. Error bars, mean ± s.d. (c) Strain - Poisson's ratio curves. (d) Stress – strain curves. (a-b) One-way ANOVA ($p < 0.05$) with Tukey's multiple comparisons tests (N = 3).

4.3.6 Cyclic tensile tests

Cyclic tensile tests were carried out to assess the mechanical durability of the pristine PCL patches and to evaluate the stability of the PVDF-HFP coating over repeated loading. Specifically, the tests aimed to determine whether the coating influenced mechanical degradation and whether it remained stable over 100 cycles. Surface damage was further examined using SEM imaging (Figure 4.17). As shown in Figure 4.16, the coated patches displayed mechanical behaviour consistent with the monotonic tensile tests, exhibiting reduced stiffness compared to the pristine patch. In particular, the Toe region extended up to approximately 20% strain, whereas in pristine patches, a transition to the second slope was already apparent at this strain. This difference led to lower stress values at 20% strain for the coated patches across all cycles. Despite this, the overall cyclic behaviour of all patches, pristine and coated, was comparable. For example, the percentage drop in peak stress across cycles was similar among the three groups. Likewise, the evolution of maximum stress per cycle, hysteresis loop area, and Toe region modulus followed the same trends. Notably, the Toe region modulus decreased from 1.9 MPa to 1.3 MPa over 100 cycles in all cases, indicating a shared softening behaviour. A particularly notable finding is the evolution of the hysteresis loop area, which quantifies the energy dissipated during each cycle. As illustrated in Figure 4.16f, the loop area decreased progressively with repeated loading, with a marked drop after the first two cycles. This behaviour suggests mechanical stabilisation over time, a characteristic feature of viscoelastic materials and some biological tissues. Indeed, studies on soft tissues have demonstrated similar patterns of cyclic response, with declining peak force over cycles [92, 93, 94]. In biomechanics, this phenomenon underlies the common practice of preconditioning, the application of repeated loading–unloading cycles to stabilise mechanical behaviour. After preconditioning, tissues typically show repeatable stress–strain curves that shift to the right [95, 96], a trend also observed in both pristine and coated patches. It should be noted, however, that this preliminary analysis involved only 100 cycles. Further testing is required to determine whether these patches exhibit long-term mechanical behaviour analogous to that of biological soft tissues.

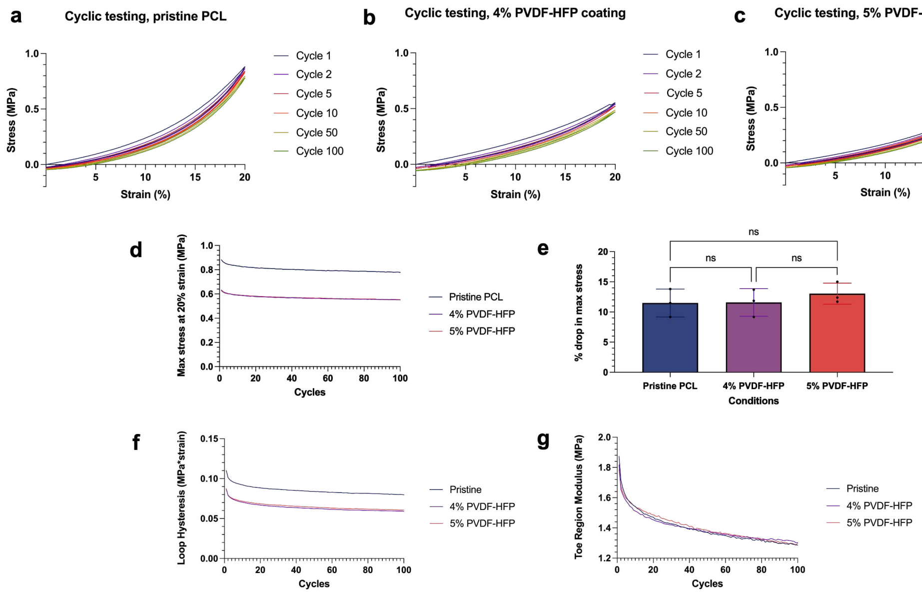

Figure 4.16: Cyclic testing of pristine PCL patches and 4% and 5% coated patches. (a) Stress – strain curves of cyclic testing of pristine PCL patches. Mean only. (b) Stress – strain curves of cyclic testing of 4% PVDF-HFP coated PCL patches. Mean only. (c) Stress – strain curves of cyclic testing of 5% PVDF-HFP coated PCL patches. Mean only. (d) Stress reached at the end of every 20% strain cycle. Mean only. (e) Drop in percentage of stress reached at the end of the first and last strain cycle. Error bars, mean ± s.d. One-way ANOVA ($p < 0.05$) with Tukey's multiple comparisons tests ($N = 3$). (f) Loop hysteresis area for each cycle. Mean only. (g) Toe region modulus for each cycle. Mean only.

4.3.7 SEM

As described in Section 3.6.2, SEM imaging was performed on all three groups, namely pristine, 4%, and 5% PVDF-HFP coated patches, under three mechanical conditions: unstrained, post monotonic loading at 40% strain, and after 100 cycles of cyclic loading at 20% strain. In the unstrained state, the 5% PVDF-HFP coating appeared more homogeneous and stable, with material clearly visible both at the fibre intersections and along the stacked layers. In contrast, the 4% coating was less uniform, primarily concentrated at intersection points and showing signs of partial detachment. The second condition, post monotonic loading at 40% strain, was selected because this strain level exceeds the Toe region, implying that fibre rotation at the intersections is mostly complete. This allowed assessment of whether such rotation caused coating detachment. Additionally, this condition was used to investigate whether plastic deformation occurred in the pristine patches.

SEM images revealed minimal changes in geometry across all samples, with only slight elongation of the lozenge structure. Some minor coating deformation and detachment were observed, particularly at the intersections, where deformation is higher, but the 5% coating remained more consistent and intact than the 4% one. After cyclic testing, no visible damage or changes in structure were observed in the pristine samples. However, both coated groups showed signs of localised damage at the intersection points, including reduced interlayer bonding and partial delamination of the top fibres, suggesting that the coating may compromise the mechanical cohesion between stacked layers under repeated strain. Since the 5% PVDF-HFP coating appeared qualitatively more stable and homogeneous across all three strain conditions compared to the 4% coating, further analyses were conducted exclusively on the 5% samples.

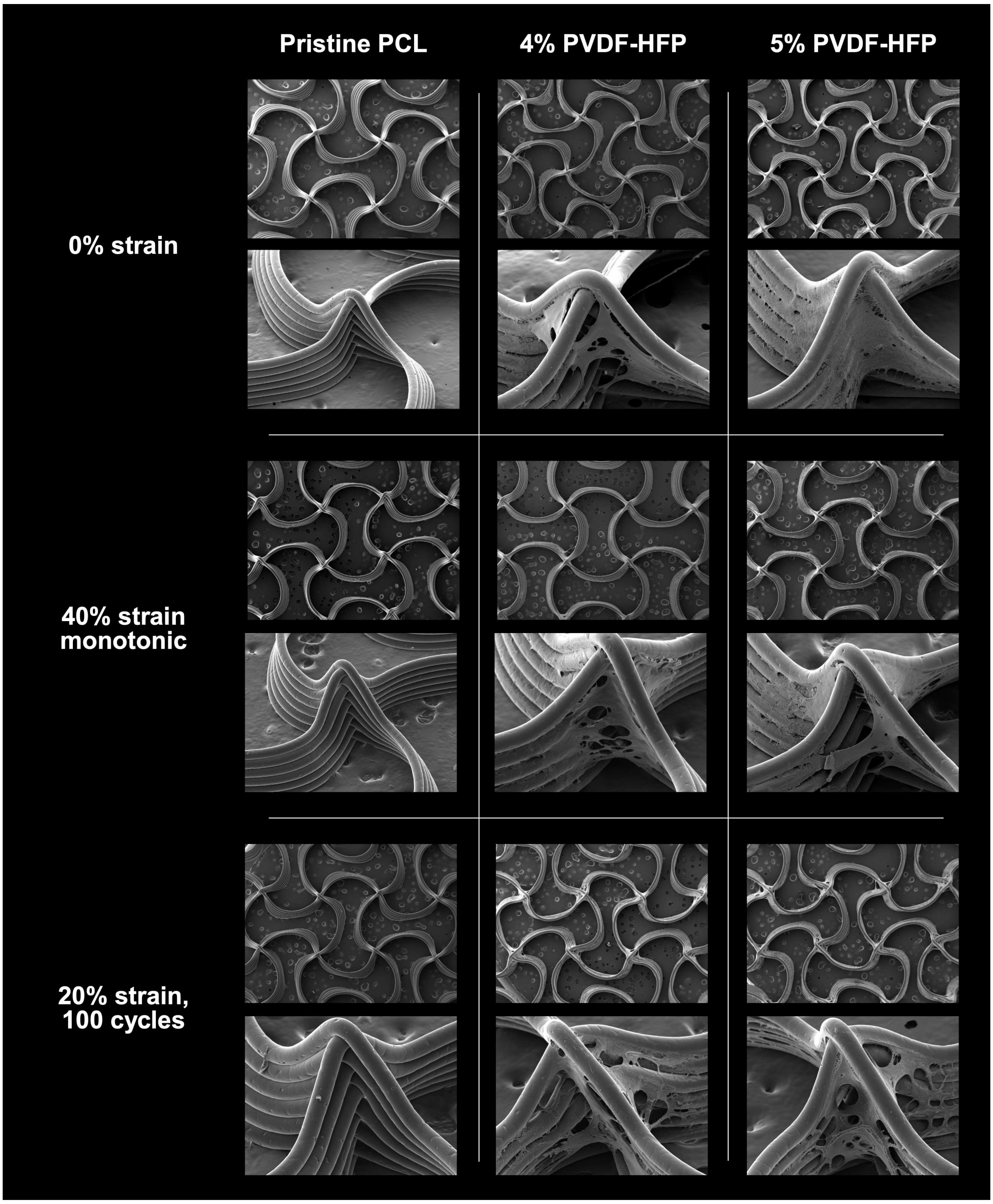

Figure 4.17: SEM images of pristine, 4%, and 5% PVDF-HFP coated patches, under three mechanical conditions: unstrained, post monotonic loading at 40% strain, and after 100 cycles of cyclic loading at 20% strain.

4.3.8 FTIR

As previously discussed, FTIR spectroscopy is a widely used method to assess piezoelectricity, particularly through the quantification of the piezoelectric β-phase [97, 98] . In this study, FTIR analysis was conducted to investigate the effect of different processing methods on β-phase content in three PVDF-based piezoelectric polymers, PVDF-HFP, Kynar 720, and Kynar 705, as well as to confirm the presence of the piezoelectric β-phase in the coated patches (Figure 4.18a). Among all tested conditions, Kynar 720 exhibited the highest increase in β-phase content (approximately 20%) following solvent casting. A similar trend was observed for solvent-cast PVDF-HFP, where the β-phase was also predominant. These findings are consistent with previous reports [99], although it is worth noting that some studies apply higher evaporation temperatures, as the crystalline phase of PVDF is closely related to the crystallisation rate of the polymer solution. Crystallisation below 70 °C has been associated with the formation of α- or γ-phases phases [100, 101]; however, other studies have reported high β-phase content even at these lower temperatures, particularly when DMF is used as a solvent [102, 103]. Since MEW processing was not feasible for Kynar 705, thermal treatment was instead applied by melting the polymer at 200 °C for 2 hours, as described in Section 3.7. This process did not increase the β-phase content, in agreement with previous literature suggesting that thermal treatment alone is insufficient. Achieving high β-phase content typically requires a combination of thermal processing and mechanical stretching [102], particularly in the presence of an electric field. This underscores the potential of MEW as a promising technique for processing piezoelectric polymers, as it can simultaneously provide thermal, mechanical, and electrical stimuli, all of which are known to promote β-phase formation [76, 89]. As shown in Figure 4.18b, FTIR analysis also confirmed the successful deposition of PVDF-HFP on the PCL patches, as indicated by the presence of characteristic PVDF peaks in the spectrum of the coated patch compared to the pristine one. Notably, the coated patches exhibited a β-phase content of approximately 76%, comparable to that of the solvent-cast PVDF-HFP (Table 4.2). This result is particularly relevant given that the patches were dried under vacuum over multiple cycles, suggesting that the evaporation rate did not significantly affect the resulting piezoelectric phase.

4.3.9 Biological assays

As shown in Figure 4.19, MTT assay results revealed distinct responses between cardiac fibroblasts and macrophages following exposure to material-conditioned media. For iPSC-derived cardiac fibroblasts, a statistically significant difference in viability was observed across all conditions. The positive control, consisting of untreated culture medium, exhibited the highest absorbance, as expected. Among the tested

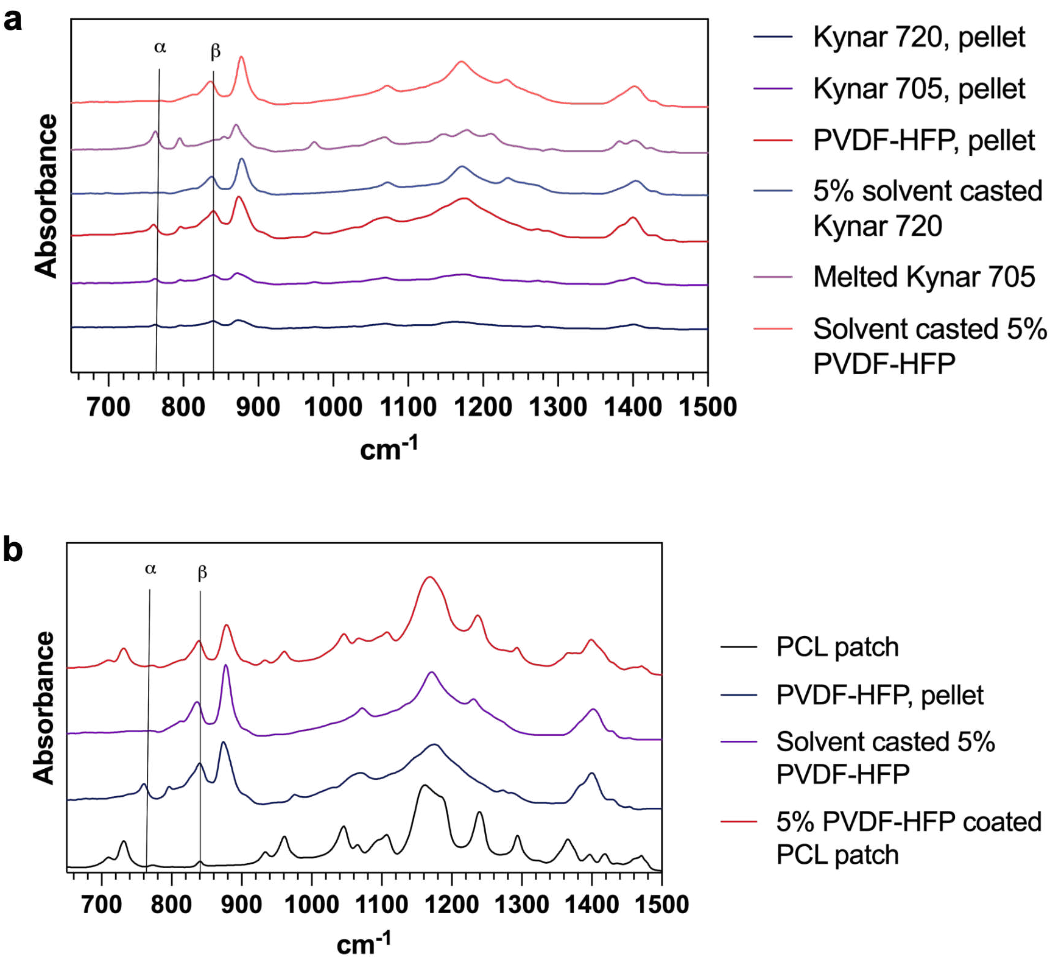

Figure 4.18: FTIR analysis

Table 4.2: Quantification of β phase

Sample	**A @ 840 cm^{-1}**	**A @ 763 cm^{-1}**	β **phase (%)**
Kynar 720, pellet	0.0338	0.0171	61.03
Kynar 705, pellet	0.0246	0.0421	31.64
PVDF-HFP, pellet	0.1322	0.0637	62.18
5% SC Kynar 720	0.0833	0.0151	81.42
Melted Kynar 705	0.0535	0.0926	31.4
5% SC PVDF-HFP	0.1075	0.0303	73.76
5% PVDF-HFP coating	0.1023	0.0259	75.79

materials, Kynar 705-conditioned medium supported higher viability than PVDF-HFP, suggesting more favourable cytocompatibility. PVDF-HFP also maintained cell viability above baseline, although to a lesser extent. The negative control, consisting of DMSO treatment, resulted in complete loss of viability, confirming the assay sensitivity. These findings suggest that both materials are non-cytotoxic to cardiac fibroblasts, with Kynar 705 potentially providing a more supportive environment for cell survival or metabolism. In contrast, macrophage viability results showed a different trend. The DMSO-treated wells again confirmed the negative control status, showing minimal absorbance. Interestingly, all other conditions, including both material-conditioned media and the positive control, resulted in significantly higher absorbance values, with no significant differences among them. This suggests that exposure to the materials did not impair macrophage viability, and may even have induced a degree of metabolic activation. However, as the MTT assay measures metabolic activity rather than specific cell function [104] , it is not possible to determine from these data alone whether this reflects increased proliferation, activation, or other cellular responses, as studies have shown that the level of MTT reduction and consequent formazan production on which the assay is based depends not only on the overall cell population viability, but also on the single cell metabolic activity [104]. Given the key role of macrophages in material-induced immune responses [105], further investigation would be necessary, including markers of activation or cytokine release, to determine whether the observed metabolic increase reflects a pro-inflammatory or pro-regenerative phenotype [106]. Overall, both PVDF-HFP and Kynar 705 demonstrated good cytocompatibility, particularly with fibroblasts. Kynar 705 appeared more favourable in supporting fibroblast viability, while neither material exhibited cytotoxic effects on macrophages. These findings support the further investigation of these materials for cardiac tissue applications, though additional assays would be required to assess immune modulation and long-term compatibility.

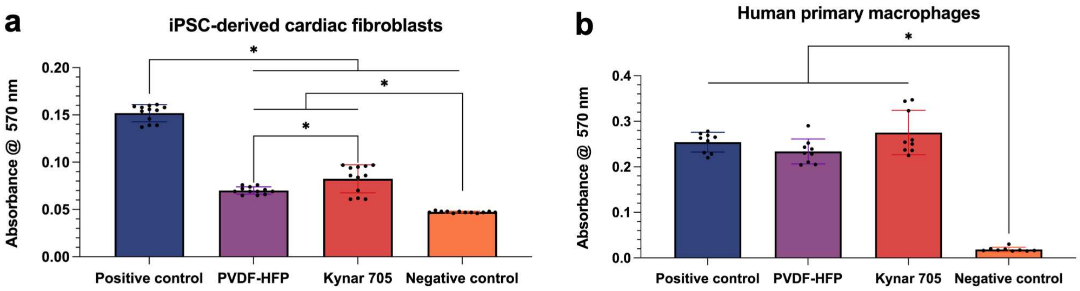

Figure 4.19: MTT assay. (a) MTT assay on iPSC-derived cardiac fibroblasts. (b) MTT assay on human primary macrophages. (a-b) One-way ANOVA ($p < 0.05$) with Tukey's multiple comparisons tests ($N = 3$).

Chapter 5

Conclusions and future perspectives

This work aimed to design, fabricate and characterise a piezoelectric and auxetic patch as a potential novel strategy for myocardial regeneration.

A framework was developed to compare auxetic geometries fabricated via MEW, using the lozenge truss design for systematic evaluation. Scaling the unit cell size significantly affected the Toe region modulus, decreasing inversely with the square of the scaling factor, consistent with literature. Neither scaling nor layer count influenced the Effective Young's Modulus, which remained material-dependent at higher strains. All designs retained negative Poisson's ratio behaviour regardless of scaling or layer count. These findings underscore the importance of defining consistent physical dimensions for comparative analysis of auxetic geometries, particularly when considering clinical applications.

The following comparative analysis of auxetic designs demonstrated the critical influence of geometry on the mechanical performance of MEW-fabricated cardiac patches. Among the tested designs, the missing rib geometry emerged as the most promising, offering a favourable balance between stiffness anisotropy and negative Poisson's ratio, both of which align closely with the mechanical behaviour of native myocardium. While the lozenge truss also exhibited a suitable Poisson's ratio, its geometric isotropy limits its applicability in replicating myocardial anisotropy. Conversely, the arrowhead design, despite its anisotropic characteristics, displayed excessive stiffness ratios and entered the plastic regime under physiologic transverse strain, rendering it unsuitable for cardiac applications.

Attempts to directly print piezoelectric scaffolds with PVDF-HFP and Kynar 705 via MEW were unsuccessful due to extrusion issues. Dip coating PCL scaffolds with 4% and 5% PVDF-HFP solutions was adopted instead to introduce piezoelectric properties to the patches.

The feasibility of fabricating auxetic scaffolds with piezoelectric properties through the integration of PVDF-based polymers using MEW and dip coating techniques was explored. Initial MEW processing attempts using PVDF-HFP and Kynar 705 were unsuccessful. PVDF-HFP could not be extruded, likely due to its high melt viscosity, whereas Kynar 705 quickly solidified after extrusion before reaching the collector plate. Coating did not alter the TRM but reduced the Effective Young's Modulus, likely due to residual solvent effects. Coated patches showed enhanced auxetic response, possibly from looser fibre interactions, with negligible mechanical differences between concentrations. Cyclic tensile tests confirmed coated patches maintained mechanical integrity, showing similar softening and hysteresis trends as uncoated patches, paralleling biological tissue preconditioning. FTIR confirmed sufficient β-phase content to ensure piezoelectric response. SEM showed the 5% coating had more uniform and stable coverage than 4%, which exhibited partial detachment after loading. These findings demonstrate that dip coating with PVDF-HFP can effectively introduce piezoelectric material to auxetic scaffolds without compromising mechanical function, supporting its suitability for future integration into regenerative applications. MTT assays with iPSC-derived cardiac fibroblasts and primary macrophages showed no cytotoxicity from PVDF-HFP or Kynar 705 conditioned media over 24 hours. While these preliminary cytotoxicity screenings highlight the potential of these materials in the biomedical field, longer-term cell studies are due in the future to fully assess biocompatibility.

While this project establishes a robust foundation for future research, it simultaneously opens numerous promising avenues for further exploration. Concerning patch geometry, advancing the fabrication process to enable printing with finer fibres will be crucial. This would facilitate the creation of smaller unit cells, bringing the designs closer to the dimensional standards commonly reported in MEW literature. A significant progression in the comparative analysis of auxetic structures would be the integration of finite element modelling. This approach could systematically investigate a broad spectrum of auxetic geometries and elucidate how their defining parameters influence key mechanical properties such as Poisson's ratio, Toe Region Modulus, and Effective Young's Modulus. Such insights would not only enhance scaffold design for cardiac regeneration but could also extend to engineering constructs for other tissues and organs.

Future efforts should also focus on optimising MEW processing of Kynar 705, potentially through the incorporation of a heated collector within the Spraybase system to overcome current fabrication challenges. Furthermore, in vivo studies are essential to deepen understanding of the effects of PVDF-based coatings on critical cell populations involved in myocardial repair, including cardiomyocytes, cardiac fibroblasts, and macrophages.

Although further characterisation is required, this preliminary study highlights piezoelectric cardiac patches with auxetic geometry as a compelling novel approach for myocardial infarction therapy. The integration of these two features within a single scaffold holds considerable promise to revolutionise the treatment of this complex biomedical condition.

Bibliography

[1] Adam Timmis et al. «European society of cardiology: the 2023 atlas of cardiovascular disease statistics». In: *European Heart Journal* 45.38 (2024), pp. 4019–4062. ISSN: 0195-668X (cit. on pp. 1, 3).

[2] World Health Organization (WHO). *Cardiovascular diseases.* Web Page. 2025. URL: `https://www.who.int/health-topics/cardiovascular-diseases#tab=tab_1` (cit. on p. 1).

[3] Olga Brazhkina, Jeong Hun Park, Hyun-Ji Park, Sruti Bheri, Joshua T Maxwell, Scott J Hollister, and Michael E Davis. «Designing a 3D printing based auxetic cardiac patch with hiPSC-CMs for heart repair». In: *Journal of Cardiovascular Development and Disease* 8.12 (2021), p. 172. ISSN: 2308-3425 (cit. on pp. 1, 10).

[4] Nikolaos G Frangogiannis. «The extracellular matrix in myocardial injury, repair, and remodeling». In: *The Journal of clinical investigation* 127.5 (2017), pp. 1600–1612. ISSN: 0021-9738 (cit. on p. 1).

[5] Signe Holm Nielsen, Alan J Mouton, Kristine Y DeLeon-Pennell, Federica Genovese, Morten Karsdal, and Merry L Lindsey. «Understanding cardiac extracellular matrix remodeling to develop biomarkers of myocardial infarction outcomes». In: *Matrix Biology* 75 (2019), pp. 43–57. ISSN: 0945-053X (cit. on p. 1).

[6] Bahareh Doustvandi, Rana Imani, and Maryam Yousefzadeh. «Study of electrospun PVDF/GO nanofibers as a conductive piezoelectric heart patch for potential support of myocardial regeneration». In: *Macromolecular Materials and Engineering* 309.1 (2024), p. 2300243. ISSN: 1438-7492 (cit. on pp. 1, 5).

[7] Marieke Rienks, Anna-Pia Papageorgiou, Nikolaos G Frangogiannis, and Stephane Heymans. «Myocardial extracellular matrix: an ever-changing and diverse entity». In: *Circulation research* 114.5 (2014), pp. 872–888. ISSN: 0009-7330 (cit. on p. 1).

[8] Jianyi Zhang, Wuqiang Zhu, Milica Radisic, and Gordana Vunjak-Novakovic. «Can we engineer a human cardiac patch for therapy?» In: *Circulation research* 123.2 (2018), pp. 244–265. ISSN: 0009-7330 (cit. on pp. 1, 4).

[9] Lei Ye, Wolfram-Hubertus Zimmermann, Daniel J Garry, and Jianyi Zhang. «Patching the heart: cardiac repair from within and outside». In: *Circulation research* 113.7 (2013), pp. 922–932. ISSN: 0009-7330 (cit. on p. 1).

[10] Maribella Domenech, Lilliana Polo-Corrales, Jaime E Ramirez-Vick, and Donald O Freytes. «Tissue engineering strategies for myocardial regeneration: acellular versus cellular scaffolds?» In: *Tissue Engineering Part B: Reviews* 22.6 (2016), pp. 438–458. ISSN: 1937-3368 (cit. on p. 1).

[11] Michaella Kapnisi et al. «Auxetic cardiac patches with tunable mechanical and conductive properties toward treating myocardial infarction». In: *Advanced functional materials* 28.21 (2018), p. 1800618. ISSN: 1616-301X (cit. on pp. 1, 4, 8, 9, 42).

[12] Parth Chansoria et al. «Rationally Designed Anisotropic and Auxetic Hydrogel Patches for Adaptation to Dynamic Organs». In: *Advanced Functional Materials* 32.43 (2022), p. 2207590. ISSN: 1616-301X. DOI: `https://doi.org/10.1002/adfm.202207590`. URL: `https://advanced.onlinelibrary.wiley.com/doi/abs/10.1002/adfm.202207590` (cit. on pp. 1, 4, 8, 11, 35, 42, 44, 47).

[13] H MA Kolken and AA Zadpoor. «Auxetic mechanical metamaterials». In: *RSC advances* 7.9 (2017), pp. 5111–5129 (cit. on p. 1).

[14] Dinorath Olvera, Mina Sohrabi Molina, Gillian Hendy, and Michael G Monaghan. «Electroconductive melt electrowritten patches matching the mechanical anisotropy of human myocardium». In: *Advanced Functional Materials* 30.44 (2020), p. 1909880. ISSN: 1616-301X (cit. on pp. 1, 2, 4, 9, 10, 44).

[15] Kenji Uchino. «The development of piezoelectric materials and the new perspective». In: *Advanced piezoelectric materials*. Elsevier, 2017, pp. 1–92 (cit. on pp. 2, 5).

[16] Hong-Feng Guo, Zhen-Sheng Li, Shi-Wu Dong, Wei-Jun Chen, Ling Deng, Yu-Fei Wang, and Da-Jun Ying. «Piezoelectric PU/PVDF electrospun scaffolds for wound healing applications». In: *Colloids and Surfaces B: Biointerfaces* 96 (2012), pp. 29–36. ISSN: 0927-7765 (cit. on pp. 2, 14).

[17] Maria Kitsara, Andreu Blanquer, Gonzalo Murillo, Vincent Humblot, Sara De Bragança Vieira, Carme Nogués, Elena Ibáñez, Jaume Esteve, and Leonardo Barrios. «Permanently hydrophilic, piezoelectric PVDF nanofibrous scaffolds promoting unaided electromechanical stimulation on osteoblasts». In: *Nanoscale* 11.18 (2019), pp. 8906–8917 (cit. on pp. 2, 14).

[18] Yuan Cheng, Yang Xu, Yun Qian, Xuan Chen, Yuanming Ouyang, and Wei-En Yuan. «3D structured self-powered PVDF/PCL scaffolds for peripheral nerve regeneration». In: *Nano Energy* 69 (2020), p. 104411. ISSN: 2211-2855 (cit. on p. 2).

[19] Nader Salari, Fatemeh Morddarvanjoghi, Amir Abdolmaleki, Shabnam Rasoulpoor, Ali Asghar Khaleghi, Leila Afshar Hezarkhani, Shamarina Shohaimi, and Masoud Mohammadi. «The global prevalence of myocardial infarction: a systematic review and meta-analysis». In: *BMC cardiovascular disorders* 23.1 (2023), p. 206. ISSN: 1471-2261 (cit. on p. 3).

[20] Grant W Reed, Jeffrey E Rossi, and Christopher P Cannon. «Acute myocardial infarction». In: *The Lancet* 389.10065 (2017), pp. 197–210. ISSN: 0140-6736 (cit. on p. 3).

[21] Marc A Pfeffer and Eugene Braunwald. «Ventricular remodeling after myocardial infarction. Experimental observations and clinical implications». In: *Circulation* 81.4 (1990), pp. 1161–1172. ISSN: 0009-7322 (cit. on p. 3).

[22] Susan A Thompson, Craig R Copeland, Daniel H Reich, and Leslie Tung. «Mechanical coupling between myofibroblasts and cardiomyocytes slows electric conduction in fibrotic cell monolayers». In: *Circulation* 123.19 (2011), pp. 2083–2093. ISSN: 0009-7322 (cit. on p. 3).

[23] Bruno R Nascimento, Luisa C Caldeira Brant, Bárbara CA Marino, Luiz Guilherme Passaglia, and Antonio Luiz P Ribeiro. «Implementing myocardial infarction systems of care in low/middle-income countries». In: *Heart* 105.1 (2019), pp. 20–26. ISSN: 1355-6037 (cit. on p. 3).

[24] Robert A Byrne et al. «2023 ESC guidelines for the management of acute coronary syndromes: developed by the task force on the management of acute coronary syndromes of the European Society of Cardiology (ESC)». In: *European Heart Journal: Acute Cardiovascular Care* 13.1 (2024), pp. 55–161. ISSN: 2048-8726 (cit. on p. 3).

[25] Eric M Small et al. «Myocardin-related transcription factor-a controls myofibroblast activation and fibrosis in response to myocardial infarction». In: *Circulation research* 107.2 (2010), pp. 294–304. ISSN: 0009-7330 (cit. on p. 4).

[26] Kilian Maria Arthur Mueller, Salma Mansi, Elena M De-Juan-Pardo, and Petra Mela. «Advances in melt electrowriting for cardiovascular applications». In: *Frontiers in Bioengineering and Biotechnology* 12 (2024), p. 1425073. ISSN: 2296-4185 (cit. on p. 4).

[27] Laura R Geuss and Laura J Suggs. «Making cardiomyocytes: how mechanical stimulation can influence differentiation of pluripotent stem cells». In: *Biotechnology progress* 29.5 (2013), pp. 1089–1096. ISSN: 8756-7938 (cit. on p. 4).

[28] Barbara Illi, Alessandro Scopece, Simona Nanni, Antonella Farsetti, Liliana Morgante, Paolo Biglioli, Maurizio C Capogrossi, and Carlo Gaetano. «Epigenetic histone modification and cardiovascular lineage programming in mouse embryonic stem cells exposed to laminar shear stress». In: *Circulation research* 96.5 (2005), pp. 501–508. ISSN: 0009-7330 (cit. on p. 4).

[29] Maike Schmelter, Bernadette Ateghang, Simone Helmig, Maria Wartenberg, and Heinrich Sauer. «Embryonic stem cells utilize reactive oxygen species as transducers of mechanical strain-induced cardiovascular differentiation». In: *Faseb Journal* 20.8 (2006). ISSN: 0892-6638 (cit. on p. 4).

[30] Maria Carlos-Oliveira, Ferran Lozano-Juan, Paola Occhetta, Roberta Visone, and Marco Rasponi. «Current strategies of mechanical stimulation for maturation of cardiac microtissues». In: *Biophysical reviews* 13.5 (2021), pp. 717–727. ISSN: 1867-2450 (cit. on p. 4).

[31] Roberto Gaetani, Eric Adriano Zizzi, Marco Agostino Deriu, Umberto Morbiducci, Maurizio Pesce, and Elisa Messina. «When stiffness matters: mechanosensing in heart development and disease». In: *Frontiers in Cell and Developmental Biology* 8 (2020), p. 334. ISSN: 2296-634X (cit. on p. 4).

[32] Antonella Silvestri, Monica Boffito, Susanna Sartori, and Gianluca Ciardelli. «Biomimetic materials and scaffolds for myocardial tissue regeneration». In: *Macromolecular bioscience* 13.8 (2013), pp. 984–1019. ISSN: 1616-5187 (cit. on pp. 4, 42).

[33] Dimitri Mojsejenko, Jeremy R McGarvey, Shauna M Dorsey, Joseph H Gorman III, Jason A Burdick, James J Pilla, Robert C Gorman, and Jonathan F Wenk. «Estimating passive mechanical properties in a myocardial infarction using MRI and finite element simulations». In: *Biomechanics and modeling in mechanobiology* 14.3 (2015), pp. 633–647. ISSN: 1617-7959 (cit. on p. 4).

[34] Qi-Zhi Chen, Sian E Harding, Nadire N Ali, Alexander R Lyon, and Aldo R Boccaccini. «Biomaterials in cardiac tissue engineering: ten years of research survey». In: *Materials Science and Engineering: R: Reports* 59.1-6 (2008), pp. 1–37. ISSN: 0927-796X (cit. on pp. 4, 42).

[35] Stefan Dhein, Thomas Seidel, Aida Salameh, Joanna Jozwiak, Anja Hagen, Martin Kostelka, Gerd Hindricks, and Friedrich-Wilhelm Mohr. «Remodeling of cardiac passive electrical properties and susceptibility to ventricular and atrial arrhythmias». In: *Frontiers in Physiology* 5 (2014), p. 424. ISSN: 1664-042X (cit. on p. 5).

[36] Mark E Anderson, Joshua Goldhaber, Steven R Houser, Michel Puceat, and Mark A Sussman. «Embryonic stem cell–derived cardiac myocytes are not ready for human trials». In: *Circulation research* 115.3 (2014), pp. 335–338. ISSN: 0009-7330 (cit. on p. 5).

[37] James JH Chong et al. «Human embryonic-stem-cell-derived cardiomyocytes regenerate non-human primate hearts». In: *Nature* 510.7504 (2014), pp. 273–277. ISSN: 0028-0836 (cit. on p. 5).

[38] Ruilian Ma et al. «Electrical stimulation enhances cardiac differentiation of human induced pluripotent stem cells for myocardial infarction therapy». In: *Antioxidants redox signaling* 28.5 (2018), pp. 371–384. ISSN: 1523-0864 (cit. on p. 5).

[39] Yue Dai, Junsheng Mu, and Fan Zhou. «The use of electrical stimulation to induce cardiac differentiation of stem cells for the treatment of myocardial infarction». In: *Reviews in Cardiovascular Medicine* 22.4 (2021), pp. 1167–1171. ISSN: 1530-6550 (cit. on p. 5).

[40] Meenakshi Suku, Jack F Murphy, Sara Corbezzolo, Manus Biggs, Giancarlo Forte, Irene C Turnbull, Kevin D Costa, Lesley Forrester, and Michael G Monaghan. «Synergistic generation of cardiac resident-like macrophages and cardiomyocyte maturation in tissue engineered platforms». In: *BioRxiv* (2024), p. 2024.12. 04.626684 (cit. on p. 5).

[41] Mariana Ramalho Gomes, Frederico Castelo Ferreira, and Paola Sanjuan-Alberte. «Electrospun piezoelectric scaffolds for cardiac tissue engineering». In: *Biomaterials advances* 137 (2022), p. 212808. ISSN: 2772-9508 (cit. on pp. 5, 11).

[42] Maria Kalogeropoulou, Anna Kracher, Pierpaolo Fucile, Silvia M Mihăilă, and Lorenzo Moroni. «Blueprints of Architected Materials: A Guide to Metamaterial Design for Tissue Engineering». In: *Advanced Materials* 36.47 (2024), p. 2408082. ISSN: 0935-9648 (cit. on pp. 5–9).

[43] Yujin Kim, Kuk Hui Son, and Jin Woo Lee. «Auxetic structures for tissue engineering scaffolds and biomedical devices». In: *Materials* 14.22 (2021), p. 6821. ISSN: 1996-1944 (cit. on pp. 6, 7).

[44] Roderic Lakes. «Foam structures with a negative Poisson's ratio». In: *Science* 235.4792 (1987), pp. 1038–1040. ISSN: 0036-8075 (cit. on p. 7).

[45] Joseph N Grima, Ruben Gatt, and Pierre-Sandre Farrugia. «On the properties of auxetic meta-tetrachiral structures». In: *physica status solidi (b)* 245.3 (2008), pp. 511–520. ISSN: 0370-1972 (cit. on p. 7).

[46] Zhenwei Wang, Congcong Luan, Guangxin Liao, Jiapeng Liu, Xinhua Yao, and Jianzhong Fu. «Progress in auxetic mechanical metamaterials: structures, characteristics, manufacturing methods, and applications». In: *Advanced Engineering Materials* 22.10 (2020), p. 2000312. ISSN: 1438-1656 (cit. on p. 8).

[47] Kelc Robi, Naranda Jakob, Kuhta Matevz, and Vogrin Matjaz. «The physiology of sports injuries and repair processes». In: *Current issues in sports and exercise medicine*. IntechOpen, 2013. ISBN: 9535110314 (cit. on p. 9).

[48] AA Damasceno et al. «Effects of maternal diabetes on male offspring: high cell proliferation and increased activity of MMP-2 in the ventral prostate». In: *Cell and Tissue Research* 358.1 (2014), pp. 257–269. ISSN: 0302-766X (cit. on p. 9).

[49] Kazuhiko Mitsuhashi, Swapan Ghosh, and Hiroshi Koibuchi. «Mathematical modeling and simulations for large-strain j-shaped diagrams of soft biological materials». In: *Polymers* 10.7 (2018), p. 715. ISSN: 2073-4360 (cit. on pp. 9, 10).

[50] Harry Ngwangwa, Fulufhelo Nemavhola, Thanyani Pandelani, Makhosasana Msibi, Israel Mabuda, Neil Davies, and Thomas Franz. «Determination of cross-directional and cross-wall variations of passive biaxial mechanical properties of rat myocardia». In: *Processes* 10.4 (2022), p. 629. ISSN: 2227-9717 (cit. on p. 9).

[51] Thanyani Pandelani, Letlhogonolo Semakane, Makhosasana Msibi, Alex G Kuchumov, and Fulufhelo Nemavhola. «Passive biaxial mechanical properties of sheep myocardium». In: *Frontiers in Bioengineering and Biotechnology* 13 (2025), p. 1549829. ISSN: 2296-4185 (cit. on p. 9).

[52] Lamei Du, Wei Shi, Han Gao, Hongxing Jia, Qiuting Zhang, Mingjie Liu, and Ye Xu. «Mechanically programmable composite metamaterials with switchable positive/negative Poisson's ratio». In: *Advanced Functional Materials* 34.22 (2024), p. 2314123. ISSN: 1616-301X (cit. on p. 9).

[53] Damia Mawad et al. «A conducting polymer with enhanced electronic stability applied in cardiac models». In: *Science advances* 2.11 (2016), e1601007. ISSN: 2375-2548 (cit. on p. 9).

[54] Biranche Tandon, Jonny J Blaker, and Sarah H Cartmell. «Piezoelectric materials as stimulatory biomedical materials and scaffolds for bone repair». In: *Acta biomaterialia* 73 (2018), pp. 1–20. ISSN: 1742-7061 (cit. on p. 11).

[55] Mude Zhu, Qingyou Liu, Wai-Yeung Wong, and Linli Xu. «Advancements in Carbon-Based Piezoelectric Materials: Mechanism, Classification, and Applications in Energy Science». In: *Advanced Materials* (2025), p. 2419970. ISSN: 0935-9648 (cit. on p. 11).

[56] Michael Smith and Sohini Kar-Narayan. «Piezoelectric polymers: theory, challenges and opportunities». In: *International Materials Reviews* 67.1 (2022), pp. 65–88. ISSN: 0950-6608 (cit. on p. 12).

[57] Khaled S Ramadan, Dan Sameoto, and Sthephane Evoy. «A review of piezoelectric polymers as functional materials for electromechanical transducers». In: *Smart Materials and Structures* 23.3 (2014), p. 033001. ISSN: 0964-1726 (cit. on p. 12).

[58] James F Tressler, Sedat Alkoy, and Robert E Newnham. «Piezoelectric sensors and sensor materials». In: *Journal of electroceramics* 2.4 (1998), pp. 257–272. ISSN: 1385-3449 (cit. on p. 12).

[59] Gary D Jones, Roger Alan Assink, Tim Richard Dargaville, Pavel Mikhail Chaplya, Roger Lee Clough, Julie M Elliott, Jeffrey W Martin, Daniel Michael Mowery, and Mathew Christopher Celina. *Characterization, performance and optimization of PVDF as a piezoelectric film for advanced space mirror concepts.* Report. Sandia National Laboratories (SNL), Albuquerque, NM, and Livermore, CA ..., 2005 (cit. on p. 12).

[60] Hamidreza Hoshyarmanesh and Yaser Maddahi. «Poling process of composite piezoelectric sensors for structural health monitoring: a pilot comparative study». In: *IEEE Sensors Letters* 2.1 (2018), pp. 1–4. ISSN: 2475-1472 (cit. on p. 12).

[61] Mahpara Habib, Iza Lantgios, and Katherine Hornbostel. «A review of ceramic, polymer and composite piezoelectric materials». In: *Journal of Physics D: Applied Physics* 55.42 (2022), p. 423002. ISSN: 0022-3727 (cit. on pp. 13, 14).

[62] Heiji Kawai. «The piezoelectricity of poly (vinylidene fluoride)». In: *Japanese journal of applied physics* 8.7 (1969), p. 975. ISSN: 1347-4065 (cit. on p. 13).

[63] S Abbrent, J Plestil, D Hlavata, Jan Lindgren, Jorgen Tegenfeldt, and Å Wendsjö. «Crystallinity and morphology of PVdF–HFP-based gel electrolytes». In: *Polymer* 42.4 (2001), pp. 1407–1416. ISSN: 0032-3861 (cit. on pp. 14, 48).

[64] Amir Hossein Rajabi, Michael Jaffe, and Treena Livingston Arinzeh. «Piezoelectric materials for tissue regeneration: A review». In: *Acta biomaterialia* 24 (2015), pp. 12–23. ISSN: 1742-7061 (cit. on p. 14).

[65] AJP Martin. «Tribo-electricity in wool and hair». In: *Proceedings of the Physical Society* 53.2 (1941), p. 186. ISSN: 0959-5309 (cit. on p. 14).

[66] Max Feughelman, Donald Lyman, Emory Menefee, and Barry Willis. «The orientation of the -helices in -keratin fibres». In: *International journal of biological macromolecules* 33.1-3 (2003), pp. 149–152. ISSN: 0141-8130 (cit. on p. 14).

[67] Daeyeong Kim, Sang A Han, Jung Ho Kim, Ju-Hyuck Lee, Sang-Woo Kim, and Seung-Wuk Lee. «Biomolecular piezoelectric materials: from amino acids to living tissues». In: *Advanced Materials* 32.14 (2020), p. 1906989. ISSN: 0935-9648 (cit. on p. 14).

[68] Namdev More and Govinda Kapusetti. «Piezoelectric material–a promising approach for bone and cartilage regeneration». In: *Medical hypotheses* 108 (2017), pp. 10–16. ISSN: 0306-9877 (cit. on p. 14).

[69] BT O'connor, HM Charlton, JD Currey, DRS Kirby, and C Woods. «Effects of electric current on bone in vivo». In: *Nature* 222.5189 (1969), pp. 162–163. ISSN: 0028-0836 (cit. on p. 14).

[70] Jack Ferrier, Stephen M Ross, Junya Kanehisa, and Jane E Aubin. «Osteoclasts and osteoblasts migrate in opposite directions in response to a constant electrical field». In: *Journal of cellular physiology* 129.3 (1986), pp. 283–288. ISSN: 0021-9541 (cit. on p. 14).

[71] Kelly L. O'Neill and Paul D. Dalton. «A Decade of Melt Electrowriting». In: *Small Methods* 7.7 (2023), p. 2201589. ISSN: 2366-9608. DOI: `https://doi.org/10.1002/smtd.202201589`. URL: `https://onlinelibrary.wiley.com/doi/abs/10.1002/smtd.202201589` (cit. on pp. 16, 31).

[72] Punam K Saha, Gunilla Borgefors, and Gabriella Sanniti di Baja. «A survey on skeletonization algorithms and their applications». In: *Pattern recognition letters* 76 (2016), pp. 3–12. ISSN: 0167-8655 (cit. on p. 23).

[73] Dingsheng Deng. «DBSCAN clustering algorithm based on density». In: *2020 7th international forum on electrical engineering and automation (IFEEA)*. IEEE, pp. 949–953. ISBN: 1728196272 (cit. on p. 23).

[74] Raul Machado and Vitor Sencadas. «Advanced techniques for characterizing bioinspired materials». In: *Bioinspired Materials for Medical Applications*. Elsevier, 2017, pp. 177–214 (cit. on p. 24).

[75] Sreelakshmi Moozhiyil Purushothaman et al. «Quantifying the crystalline polymorphism in PVDF: comparative criteria using DSC, WAXS, FT-IR, and Raman spectroscopy». In: *ACS Applied Polymer Materials* 6.14 (2024), pp. 8291–8305. ISSN: 2637-6105 (cit. on p. 26).

[76] Sammy Florczak, Thomas Lorson, Tian Zheng, Miroslav Mrlik, Dietmar W Hutmacher, Michael J Higgins, Robert Luxenhofer, and Paul D Dalton. «Melt electrowriting of electroactive poly (vinylidene difluoride) fibers». In: *Polymer International* 68.4 (2019), pp. 735–745. ISSN: 0959-8103 (cit. on pp. 26, 58).

[77] Xiaomei Cai, Tingping Lei, Daoheng Sun, and Liwei Lin. «A critical analysis of the , and phases in poly (vinylidene fluoride) using FTIR». In: *RSC advances* 7.25 (2017), pp. 15382–15389 (cit. on p. 26).

[78] Wanessa Sales de Almeida and Durcilene Alves da Silva. «Does polysaccharide quaternization improve biological activity?» In: *International journal of biological macromolecules* 182 (2021), pp. 1419–1436. ISSN: 0141-8130 (cit. on p. 27).

[79] Sinead A O'Rourke, Nuno GB Neto, Eimear Devilly, Lianne C Shanley, Hannah K Fitzgerald, Michael G Monaghan, and Aisling Dunne. «Cholesterol crystals drive metabolic reprogramming and M1 macrophage polarisation in primary human macrophages». In: *Atherosclerosis* 352 (2022), pp. 35–45. ISSN: 0021-9150 (cit. on p. 27).

[80] Jianhua Zhang et al. «Functional cardiac fibroblasts derived from human pluripotent stem cells via second heart field progenitors». In: *Nature Communications* 10.1 (2019), p. 2238. ISSN: 2041-1723. DOI: `10.1038/s41467-019-09831-5`. URL: `https://doi.org/10.1038/s41467-019-09831-5` (cit. on p. 28).

[81] Kang Han, Mao Mao, Liyan Fu, Yabo Zhang, Yuming Kang, Dichen Li, and Jiankang He. «Multimaterial Printing of Serpentine Microarchitectures with Synergistic Mechanical/Piezoelectric Stimulation for Enhanced Cardiac-Specific Functional Regeneration». In: *Small* 20.42 (2024), p. 2401561. ISSN: 1613-6810 (cit. on p. 31).

[82] Zhongfei Zou, Yu Wang, Zhen Shen, and Nan Luo. «Study on suppression strategy of jet lag effect in melt electrowriting». In: *Journal of Mechanical Science and Technology* 37.9 (2023), pp. 4801–4808. ISSN: 1738-494X (cit. on p. 31).

[83] Samuel T Wall, Joseph C Walker, Kevin E Healy, Mark B Ratcliffe, and Julius M Guccione. «Theoretical impact of the injection of material into the myocardium: a finite element model simulation». In: *Circulation* 114.24 (2006), pp. 2627–2635. ISSN: 0009-7322 (cit. on p. 42).

[84] Luiz Francisco Malmonge, José Antonio Malmonge, and Walter Katsumi Sakamoto. «Study of pyroelectric activity of PZT/PVDF-HFP composite». In: *Materials Research* 6 (2003), pp. 469–473. ISSN: 1516-1439 (cit. on pp. 47, 48).

[85] Juliane C Kade and Paul D Dalton. «Polymers for melt electrowriting». In: *Advanced healthcare materials* 10.1 (2021), p. 2001232. ISSN: 2192-2640 (cit. on pp. 47, 48).

[86] Lixin Yang, Guoping Zhang, Yi Lou, Zhihua Jiang, and Lei Du. «Melt Electrowriting of High-Quality Poly (vinylidene fluoride) Scaffolds Through Optimized Charge-Neutralization Strategy». In: *Fibers and Polymers* (2025), pp. 1–10. ISSN: 1229-9197 (cit. on p. 48).

[87] Huaizhong Xu, Shunsaku Fujiwara, Lei Du, Ievgenii Liashenko, Simon Luposchainsky, and Paul D Dalton. «Accessible melt electrowriting three-dimensional printer for fabricating high-precision scaffolds». In: *Polymer* 309 (2024), p. 127466. ISSN: 0032-3861 (cit. on p. 48).

[88] Xixi Wu, Wenjian Li, Lara Herlah, Marcus Koch, Hui Wang, Romana Schirhagl, and Małgorzata K Włodarczyk-Biegun. «Melt electrowritten poly-lactic acid/nanodiamond scaffolds towards wound-healing patches». In: *Materials Today Bio* 26 (2024), p. 101112. ISSN: 2590-0064 (cit. on p. 48).

[89] Juliane C. Kade, Paul F. Otto, Robert Luxenhofer, and Paul D. Dalton. «Melt electrowriting of poly(vinylidene difluoride) using a heated collector». In: *Polymers for Advanced Technologies* 32.12 (2021), pp. 4951–4955. ISSN: 1042-7147. DOI: `https://doi.org/10.1002/pat.5463`. URL: `https://onlinelibrary.wiley.com/doi/abs/10.1002/pat.5463` (cit. on pp. 48, 58).

[90] Kinyas Polat. «Energy harvesting from a thin polymeric film based on PVDF-HFP and PMMA blend». In: *Applied Physics A* 126 (2020), pp. 1–8. ISSN: 0947-8396 (cit. on p. 48).

[91] Gianluca Balzamo, Xiyu Zhang, Wolfram A Bosbach, and Elisa Mele. «In-situ formation of polyvinylidene fluoride microspheres within polycaprolactone electrospun mats». In: (2020) (cit. on p. 52).

[92] H Eshel and Y Lanir. «Effects of strain level and proteoglycan depletion on preconditioning and viscoelastic responses of rat dorsal skin». In: *Annals of Biomedical Engineering* 29 (2001), pp. 164–172. ISSN: 0090-6964 (cit. on p. 54).

[93] Ariel Sverdlik and Yoram Lanir. «Time-dependent mechanical behavior of sheep digital tendons, including the effects of preconditioning». In: *J. Biomech. Eng.* 124.1 (2002), pp. 78–84. ISSN: 0148-0731 (cit. on p. 54).

[94] Kyle P Quinn and Beth A Winkelstein. «Preconditioning is correlated with altered collagen fiber alignment in ligament». In: (2011). ISSN: 0148-0731 (cit. on p. 54).

[95] Ryley A Macrae, Karol Miller, and Barry J Doyle. «Methods in mechanical testing of arterial tissue: a review». In: *Strain* 52.5 (2016), pp. 380–399. ISSN: 0039-2103 (cit. on p. 54).

[96] Monica E Susilo, Jeffrey A Paten, Edward A Sander, Thao D Nguyen, and Jeffrey W Ruberti. «Collagen network strengthening following cyclic tensile loading». In: *Interface focus* 6.1 (2016), p. 20150088. ISSN: 2042-8898 (cit. on p. 54).

[97] LN Sim, SR Majid, and AK Arof. «FTIR studies of PEMA/PVdF-HFP blend polymer electrolyte system incorporated with LiCF3SO3 salt». In: *Vibrational Spectroscopy* 58 (2012), pp. 57–66. ISSN: 0924-2031 (cit. on p. 58).

[98] Sammy Florczak, Thomas Lorson, Tian Zheng, Miroslav Mrlik, Dietmar W Hutmacher, Michael J Higgins, Robert Luxenhofer, and Paul D Dalton. «Melt electrowriting of electroactive poly(vinylidene difluoride) fibers». In: *Polymer International* 68.4 (2019), pp. 735–745. ISSN: 0959-8103. DOI: `https://doi.org/10.1002/pi.5759`. URL: `https://scijournals.onlinelibrary.wiley.com/doi/abs/10.1002/pi.5759` (cit. on p. 58).

[99] Miray Yasar, Patrick Hassett, Neal Murphy, and Alojz Ivankovic. « phase optimization of solvent cast PVDF as a function of the processing method and additive content». In: *ACS omega* 9.24 (2024), pp. 26020–26029. ISSN: 2470-1343 (cit. on p. 58).

[100] Youn Jung Park, Yong Soo Kang, and Cheolmin Park. «Micropatterning of semicrystalline poly (vinylidene fluoride)(PVDF) solutions». In: *European polymer journal* 41.5 (2005), pp. 1002–1012. ISSN: 0014-3057 (cit. on p. 58).

[101] Marcel Benz and William B Euler. «Determination of the crystalline phases of poly (vinylidene fluoride) under different preparation conditions using differential scanning calorimetry and infrared spectroscopy». In: *Journal of applied polymer science* 89.4 (2003), pp. 1093–1100. ISSN: 0021-8995 (cit. on p. 58).

[102] Rinaldo Gregorio Jr. «Determination of the , , and crystalline phases of poly (vinylidene fluoride) films prepared at different conditions». In: *Journal of applied polymer science* 100.4 (2006), pp. 3272–3279. ISSN: 0021-8995 (cit. on p. 58).

[103] Rinaldo Gregorio Jr and Daniel Sousa Borges. «Effect of crystallization rate on the formation of the polymorphs of solution cast poly (vinylidene fluoride)». In: *Polymer* 49.18 (2008), pp. 4009–4016. ISSN: 0032-3861 (cit. on p. 58).

[104] Mahshid Ghasemi, Tyron Turnbull, Sonia Sebastian, and Ivan Kempson. «The MTT assay: utility, limitations, pitfalls, and interpretation in bulk and single-cell analysis». In: *International journal of molecular sciences* 22.23 (2021), p. 12827. ISSN: 1422-0067 (cit. on p. 61).

[105] Zeeshan Sheikh, Patricia J Brooks, Oriyah Barzilay, Noah Fine, and Michael Glogauer. «Macrophages, foreign body giant cells and their response to implantable biomaterials». In: *Materials* 8.9 (2015), pp. 5671–5701. ISSN: 1996-1944 (cit. on p. 61).

[106] Kara L Spiller and Timothy J Koh. «Macrophage-based therapeutic strategies in regenerative medicine». In: *Advanced drug delivery reviews* 122 (2017), pp. 74–83. ISSN: 0169-409X (cit. on p. 61).